

1           **Precipitating electron energy spectra and auroral**  
2           **power estimation by incoherent scatter radar with high**  
3           **temporal resolution**

4           **Habtamu W. Tesfaw**<sup>1</sup>, **Ilkka I. Virtanen**<sup>1</sup>, **Anita Aikio**<sup>1</sup>, **Amoré Nel**<sup>2</sup>, **Michael**  
5           **Kosch**<sup>2,3,4</sup>, and **Yasunobu Ogawa**<sup>5</sup>

6                           <sup>1</sup>Space Physics and Astronomy Research Unit, University of Oulu, Oulu, Finland

7                           <sup>2</sup>South African National Space Agency, Hermanus, South Africa

8                           <sup>3</sup>Physics Dept., Lancaster University, Lancaster, UK

9                           <sup>4</sup>Dept. of Physics and Astrophysics, University of Western Cape, Bellville, South Africa

10                           <sup>5</sup>National Institute of Polar Research, Tokyo, Japan

11           **Key Points:**

- 12           • We use the BAFIM-ELSPEC analysis combination to calculate the energy spec-  
13           tra of precipitating electrons with high time resolution.
- 14           • Using the fitted electron density data in precipitation events leads to wider en-  
15           ergy spectra, and larger auroral power and FAC estimates.
- 16           • Auroral power calculated using the BAFIM-ELSPEC analysis correlates well with  
17           the 427.8 nm emission line intensity.

---

Corresponding author: Habtamu W. Tesfaw, [Habtamu.Tesfaw@oulu.fi](mailto:Habtamu.Tesfaw@oulu.fi)

18 **Abstract**

19 This study presents an improved method to estimate differential energy flux, au-  
 20 roral power and field-aligned current of electron precipitation from incoherent scatter radar  
 21 data. The method is based on a newly developed data analysis technique that uses Bayesian  
 22 filtering to fit altitude profiles of electron density, electron temperature, and ion temper-  
 23 ature to observed incoherent scatter spectra with high time and range resolutions. The  
 24 electron energy spectra are inverted from the electron density profiles. Previous high-  
 25 time resolution fits have relied on the raw electron density, which is calculated from the  
 26 backscattered power assuming that the ion and electron temperatures are equal. The im-  
 27 proved technique is applied to one auroral event measured by the EISCAT UHF radar  
 28 and it is demonstrated that the effect of electron heating on electron energy spectra, au-  
 29 roral power and upward field-aligned current can be significant at times. Using the fit-  
 30 ted electron densities instead of the raw ones may lead to wider electron energy spec-  
 31 tra and auroral power up to 75% larger. The largest differences take place for precip-  
 32 itation that produces enhanced electron heating in the upper E region, and in this study  
 33 correspond to fluxes of electrons with peak energies from 3 to 5 keV. Finally, the auro-  
 34 ral power estimates are verified by comparison to the 427.8 nm auroral emission inten-  
 35 sity, which show good correlation. The improved method makes it possible to calculate  
 36 unbiased estimates of electron energy spectra with high time resolution and thereby to  
 37 study rapidly varying aurora.

38 **1 Introduction**

39 Electron precipitation to the high-latitude ionosphere is a key process in magnetosphere-  
 40 ionosphere coupling and in the physics of the mesosphere-lower thermosphere (MLT) re-  
 41 gion, because the precipitating electrons carry electric current, transfer energy from the  
 42 magnetosphere to the ionosphere, ionize neutral atoms and molecules, cause optical au-  
 43 roral emissions, heat the electron gas, and change the ion composition. High resolution  
 44 observations are needed in studies of these phenomena, as the processes often take place  
 45 in small spatial and temporal scales.

46 Electron precipitation is quantitatively characterized by the energy distribution of  
 47 the primary electrons. Electron acceleration processes in the magnetosphere that lead  
 48 to different energy spectral shapes are discussed by Newell et al. (2009) and Dombeck  
 49 et al. (2018). For a known differential energy flux, altitude profiles of ion production rate  
 50 and auroral emission rates can be determined if the neutral atmospheric parameters are  
 51 known (Rees, 1963; Fang et al., 2010).

52 Indirect estimation of the differential energy flux from electron density altitude pro-  
 53 files observed with an incoherent scatter radar (ISR) is an efficient way to observe elec-  
 54 tron precipitation from ground (Vondrak & Baron, 1977; Kirkwood, 1988; Brekke et al.,  
 55 1989; Semeter & Kamalabadi, 2005; Kaeppler et al., 2015; Simon Wedlund et al., 2013;  
 56 Virtanen et al., 2018). Unlike in situ observations with fast moving satellites and rock-  
 57 ets, the radar observations allow one to follow the time evolution of the electron precip-  
 58 itation along the local geomagnetic field.

59 Two different analysis techniques are commonly used to obtain electron densities  
 60 from an ISR observation. Scaling the backscattered power with radar system param-  
 61 eters results in the so-called raw electron density ( $N_r$ ), which is equal to the actual elec-  
 62 tron density ( $N_e$ ) if electron and ion temperatures are equal. A more sophisticated way  
 63 is to make a least-squares fit of a parametric incoherent scatter spectrum model to the  
 64 observed spectra. Typically, electron density ( $N_e$ ), electron temperature ( $T_e$ ), ion tem-  
 65 perature ( $T_i$ ), and line-of-sight ion bulk velocity ( $V_i$ ) are fitted.

66 The electron density profiles need to be observed with high resolutions in range and  
 67 time to enable accurate estimation of the rapidly varying electron energy spectra. While  
 68 plasma parameter fits to EISCAT ISR data are typically made with a few kilometer range  
 69 resolution and some tens of seconds time resolution using the Grand Unified Incoher-  
 70 ent Scatter Design and Analysis Package (GUISDAP) (Lehtinen & Huuskonen, 1996),  
 71 the electron energy spectra fits require range resolution better than 2 km (Semeter &  
 72 Kamalabadi, 2005) and time resolution of the order of five seconds (Virtanen et al., 2018).

73 Since other high-latitude ISR facilities cannot produce better resolutions either, previ-  
 74 ous high time resolution energy spectrum fits have been based on raw electron den-  
 75 sities (Burns et al., 1990; Lanchester et al., 1994, 1996, 1997; Semeter & Kamalabadi,  
 76 2005; Dahlgren et al., 2011; Virtanen et al., 2018), while the fitted electron densities have  
 77 been used with 1 min or coarser resolutions (Hargreaves & Devlin, 1990; Kirkwood &  
 78 Eliasson, 1990; Strickland et al., 1994; Fujii et al., 1995; Osepian & Kirkwood, 1996; Kosch  
 79 et al., 2001; Kaeppler et al., 2015). However, the electron precipitation tends to heat the  
 80 electron gas, which makes the implicit assumption of  $T_e = T_i$  questionable in calcula-  
 81 tion of  $N_r$ . The raw density  $N_r$  is smaller than the actual density  $N_e$  if  $T_e > T_i$ , which  
 82 may lead to underestimation of the precipitating energy flux if  $N_r$  is used in electron en-  
 83 ergy spectrum fits.

84 An optical signature of the electron precipitation are auroral emissions, which are  
 85 produced when excited atoms, molecules, and ions return to their ground states. Op-  
 86 tical observations are vital to complement the radar observations and to put them into  
 87 wider context. While optical observations lack the altitude information provided by radars,  
 88 they can image the auroral emissions in 2D and can reach angular and time resolutions  
 89 superior to those of the radars. Energy flux of the precipitating electrons can also be in-  
 90 ferred from the auroral blue line (427.8 nm) emission intensity which is emitted by re-  
 91 laxation of excited  $N_2^+$  molecular ions. Previous studies have shown direct proportion-  
 92 ality between line of sight integrated blue line emission intensity and total energy flux  
 93 of the precipitating electrons (Omholt, 1971; Rees & Luckey, 1974; Strickland et al., 1989;  
 94 Partamies et al., 2004).

95 The 427.8 nm emission intensity and auroral power inverted from radar data showed  
 96 good correlation in a study by Kaeppler et al. (2015), who used fitted electron density  
 97 data with 4.5 km range, and 1 and 3 min time resolutions. The coarse resolutions were  
 98 justified since the authors concentrated on stable auroral features. To study dynamic small-  
 99 scale structures with sub-second resolution, raw electron density profiles were combined  
 100 with optical observations by Lanchester et al. (1997). They found a good correlation be-  
 101 tween the radar and optical data when fields of view of both instruments were uniformly  
 102 filled with the observed aurora. Large fluxes found in their event were within extremely  
 103 narrow features that did not fill the fields of view of the instruments, making the com-  
 104 parison at these scales complex. More recently, Tuttle et al. (2014) reported underes-  
 105 timation of energy flux estimated from radar data when an auroral feature narrower than  
 106 the radar beam was observed.

107 The aim of this study is to introduce an improved method to calculate energy spec-  
 108 tra of auroral electrons from ISR measurements with high time resolution. We perform  
 109 full four-parameter fits to the observed incoherent scatter spectra with high resolutions  
 110 in time and range and use the actual fitted  $N_e$  in high-resolution electron energy spec-  
 111 trum inversion for the first time. Using the fitted electron density in the inversion re-  
 112 moves a bias in the fitted energy spectra that occurs during electron heating events if  
 113 the raw electron density is used.

114 The high-resolution plasma parameter fit is possible with the newly developed Bayesian  
 115 Filtering Module (BAFIM) (Virtanen et al., 2021). BAFIM makes use of smoothness pri-  
 116 ors in time and range (along the geomagnetic field line) for the plasma temperature pro-  
 117 files to reach high resolution in the electron density fits, as described in Section 4.1. Elec-

118 tron energy spectra are then inverted from the BAFIM-fitted electron density profiles  
 119 using a method developed by Virtanen et al. (2018) known as ELSPEC (ELectron SPEC-  
 120 trum) and described in Section 4.3. ELSPEC uses parametric models for the electron  
 121 energy spectra, models the ion production and loss rates, and solves the electron den-  
 122 sity as function of time from its continuity equation. Difference between the modeled elec-  
 123 tron density profile and the radar observation is then iteratively minimized to find the  
 124 best matching electron energy spectra.

125 The BAFIM-ELSPEC analysis combination is applied to an auroral event that com-  
 126 prises wide range of auroral features. By comparing the ELSPEC analysis results ob-  
 127 tained from the fitted and raw electron densities, we study effects of enhanced electron  
 128 heating on the calculated energy spectra of the precipitating electrons. To validate our  
 129 auroral power estimates, we compare the auroral power (total energy flux) calculated from  
 130 the BAFIM-ELSPEC analysis combination with that of the 427.8 nm spectral (blue) line  
 131 emission intensity.

132 The paper is organized as follows; data and measurements are introduced in Sec-  
 133 tion 2, the auroral event is described in Section 3, the radar data analysis and the ef-  
 134 fect of electron heating are discussed in Section 4, and auroral power derived from the  
 135 radar observations is compared to optical observations in Section 5. Discussion and sum-  
 136 mary are presented in Section 6.

## 137 2 Data and Measurements

138 The active auroral event presented in this study took place on 9 March 2016, 19:40  
 139 - 23:40 UT over Tromsø, Norway. The EISCAT UHF radar near Tromsø (69.58°N, 19.23°E  
 140 Geodetic, and 66.67°N, 101.41°E Geomagnetic) was pointed along the local geomagnetic  
 141 field and it was running the 'arc1' experiment, which uses a 64-bit alternating code se-  
 142 quence (Lehtinen & Häggström, 1987) with 6  $\mu$ s bit length. The 128 pulses of the code  
 143 sequence were transmitted with 3.468 ms inter-pulse periods, and autocorrelation func-  
 144 tion data decoded to 900 m range resolution were stored from each 443.9 ms long pulse  
 145 sequence. In this study we use data integrated to 4 s time resolution.

146 In addition to the ISR observations, we characterize the dynamics of the observed  
 147 auroral structures using all-sky camera (ASC) and narrow field of view optical observa-  
 148 tions. All-sky images of the auroral green line emission (557.7 nm) with 1 s time reso-  
 149 lution are obtained from the Watec monochromatic imager (WMI) (Ogawa et al., 2020)  
 150 located at the EISCAT Tromsø radar site. In addition, we use an EMCCD imager lo-  
 151 cated at the radar site (Nel et al., 2021) for narrow field of view (FoV) observations of  
 152 small-scale auroral structures around and within the radar beam. The detector images  
 153 auroral emissions at wavelength 427.8 nm with a 30° FoV and 3 s exposure time. The  
 154 camera system was pointing to the geomagnetic zenith.

155 Local and global (Nose et al., 2015) auroral electrojet indices are also used to mon-  
 156 itor the geomagnetic activity. Geomagnetic field data obtained from the IMAGE net-  
 157 work of magnetometers are used to derive the local auroral electrojet (IL) index (Kallio  
 158 et al., 2000). Finally, an induction coil magnetometer at Kilpisjärvi ( 69.06°N, 20.77°E  
 159 Geodetic, and 66.07°N, 102.30°E Geomagnetic) is used to monitor the geomagnetic pul-  
 160 sation activity (Raita & University of Oulu, 2022).

## 161 3 Event Description

162 Overview of the event is given in Figure 1. A time lapse video of the ASC and nar-  
 163 row FoV auroral images is provided as a supplementary material. The raw electron den-  
 164 sity obtained from the EISCAT UHF radar observation is placed in the first panel of the  
 165 figure. Keograms produced from the North-South cut of the narrow FoV and ASC au-

166 roral images over the radar zenith are shown in the second and third panels, respectively.  
 167 We make coordinate transformation at 110 km to calculate the latitudes for the keograms.  
 168 The horizontal white lines in the keograms represent position of the radar beam. Power  
 169 spectra of geomagnetic pulsations, and local (IL) and global (AL) auroral electrojet indices  
 170 are shown in the fourth and fifth panels, respectively. Selected all-sky auroral images  
 171 are shown in Figure 2. Magnetic midnight at Tromsø is at about 21:30 UT.

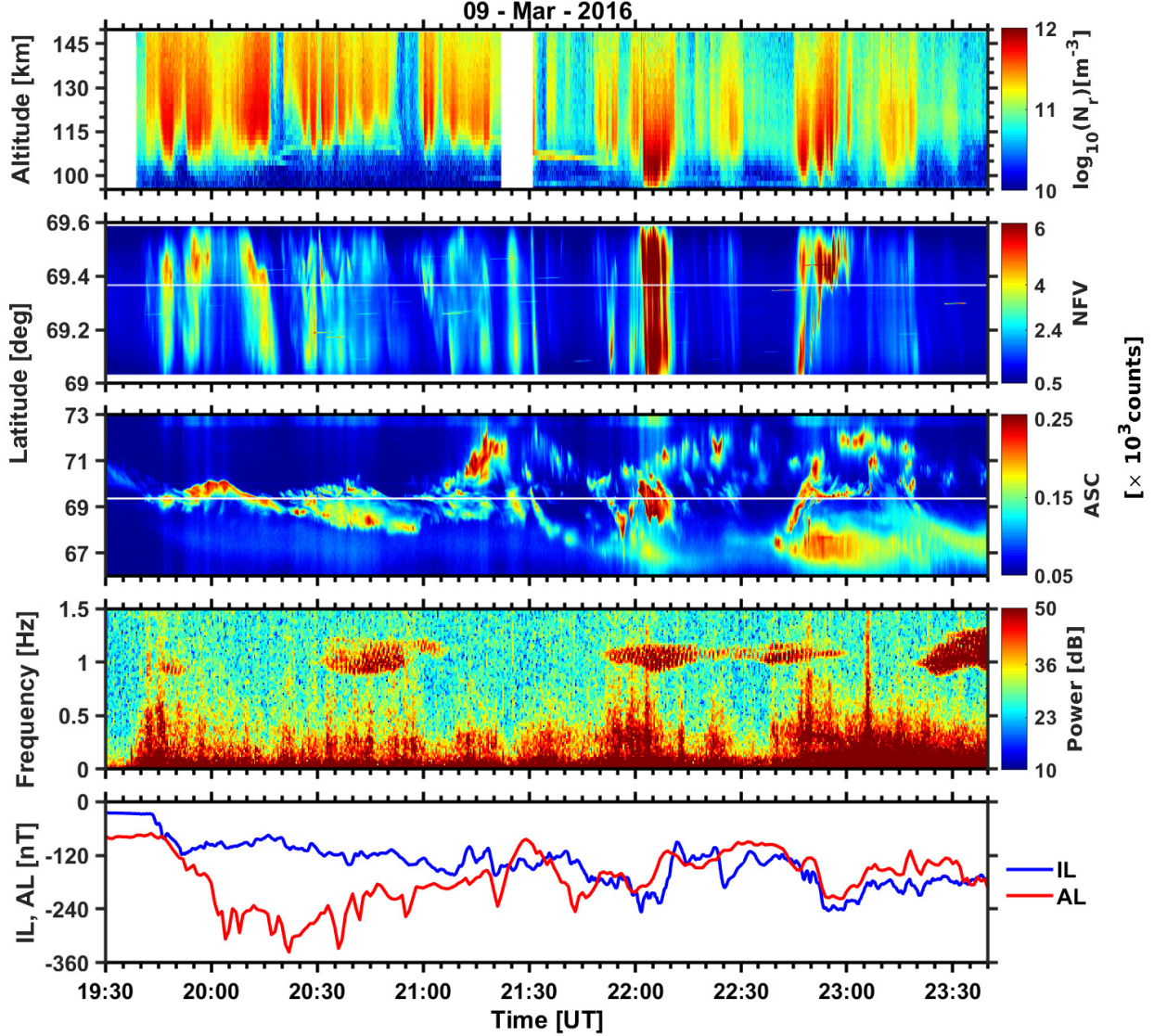


**Figure 1.** An overview of the auroral event. Panels from top to bottom: raw electron density, narrow FoV keogram (427.8 nm), ASC Keogram (557.7 nm), geomagnetic pulsation spectrogram, and IL and AL electrojet indices.

172 At 19:30 UT there were several faint arcs in the FoV of the ASC which later drifted  
 173 equatorward. After few minutes, at about 19:39 UT, the first signature of an intensifi-  
 174 cation of an arc is seen in the eastern horizon. At about the same time, the peak frequency  
 175 in the pulsation power spectrum jumps from below 1 mHz to about 0.5 Hz, which in-

176 dicates development of PiB pulsations (McPherron, 2005; Olson, 1999). PiB pulsation  
 177 development and sudden brightening of auroral arcs are typical indicators of substorm  
 178 activation (Sakurai & Saito, 1976; Mishin et al., 2020). The IL and AL indices decrease  
 179 abruptly at about 19:40, which is another indication of substorm onset (Tanskanen, 2009;  
 180 Hsu & McPherron, 2012).

181 Based on the AL index, three relatively small substorm onsets took place during  
 182 the studied time interval with rough onset times at 19:40, 21:30 and 22:40 UT. During  
 183 the first substorm, the IL index remained much smaller than the AL index indicating  
 184 that the substorm onset region was not in Scandinavia, but rather to the east, closer to  
 185 magnetic midnight.

186 In addition to the continuous PiB activity, magnetic pulsations show signatures of  
 187 Pc1 pulsations near 1 Hz, which are produced by protons injected to the inner magne-  
 188 tosphere and interacting with ion cyclotron waves (Saito, 1969). It is probable that this  
 189 injection is a consequence of substorm onset.

190 The radar starts recording large ionization enhancements after 19:44 UT when the  
 191 auroral arcs in the vicinity of the radar beam start to intensify. The radar beam was in-  
 192 side a broad luminous region with multiple bright arcs until 19:51 UT, as shown in au-  
 193 roral images A and B of Figure 2, and the radar observes the first period of enhanced  
 194 ionization between 19:44 and 19:51 UT. Intensity of the arcs in the radar beam then fade,  
 195 and by 19:52 UT they are substituted by several east-west aligned arcs forming together  
 196 a bright bulge that expands poleward. Selected images of the bulge are shown in pan-  
 197 els C and D of Figure 2.

198 Probing the poleward advancing bulge, the radar measures an ionization enhance-  
 199 ment between 19:52 and 20:00 UT. The bulge leaves the radar beam at about 20:01 UT  
 200 and continues expanding poleward until 20:04 UT. Then it starts to retreat from its pole-  
 201 ward extent and advances equatorward across the radar beam. As indicated in auroral  
 202 images E and F of Figure 2, the radar was observing the equatorward moving arc be-  
 203 tween 20:07 and 20:16 UT to produce the third ionization enhancement. The east-west  
 204 aligned arc continued drifting equatorward and left the radar beam at about 20:16:30 UT.

205 At about 20:22 UT, the AL index attained its minimum value of about -350 nT,  
 206 indicating the end of the first substorm expansion phase. During the first substorm re-  
 207 covery phase, between 20:20 and 21:30, multiple auroral features with folds and curls are  
 208 created across the auroral oval as shown in the ASC and narrow FoV keograms in Fig-  
 209 ure 1. Sample auroral images taken from this time interval are shown in panels G and  
 210 H of Figure 2. When these auroral structures perform radar beam crossings, series of sev-  
 211 eral short lived ionization enhancements are produced between 20:20 and 21:20 UT.

212 During the first substorm, all the arcs were streaming mostly towards the west. Counter-  
 213 streaming arcs were also observed so that in the northern part the streaming was to the  
 214 east and in the southern part towards the west, indicating converging electric field struc-  
 215 ture and auroral potential drop above the ionosphere (Carlson et al., 1998; Aikio et al.,  
 216 2002). We also find the energy spectra of the electron flux corresponding to these arcs  
 217 to be in the form of inverted-V type structures.

218 Following break up of the second substorm at about 21:30 UT, a bright auroral fea-  
 219 ture is seen in the north-west horizon of the ASC at about 21:35 UT, indicating the on-  
 220 set region of this substorm was to the west of Tromsø. After the onset, the streaming  
 221 inside the arcs becomes mainly eastward. Eventually a bright auroral bulge, expanding  
 222 to the ASC FoV from the west, is formed at about 21:57 UT. Selected images of the bulge  
 223 are shown in panels I and J of Figure 2. When the bulge passes through the radar beam  
 224 at about 21:59, it produces an electron density enhancement characterized by largest peak  
 225 electron densities (in the order of  $10^{12} \text{ m}^{-3}$ ) and lowest peak altitudes (about 100 km)  
 226 of the event. The narrow FoV and ASC keograms show that the radar beam was at the

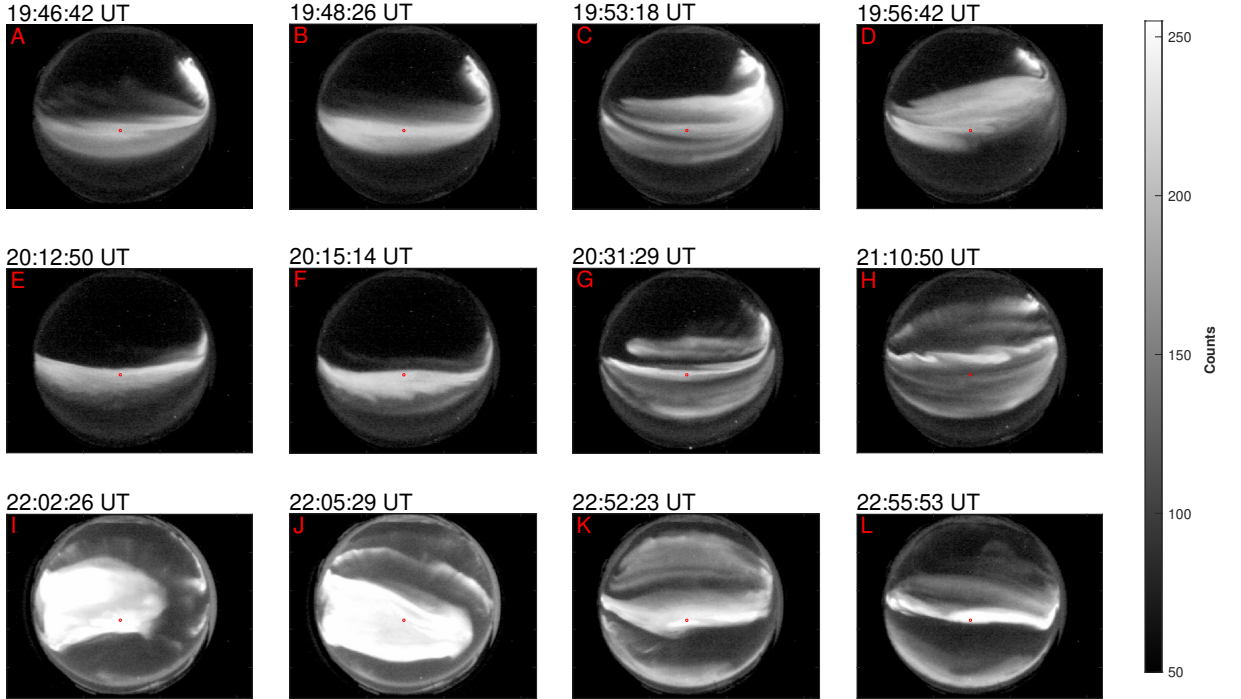


**Figure 2.** Selected auroral images taken from the ASC camera observation on 9 March, 2016. The radar beam is shown as a red dot in the images. North is up and east is to the right.

227  
228  
229

center of this intensifying bulge from 22:00 until 22:11 UT. The auroral bulge fades in its intensity by 22:12. After that and until 22:40 several auroral features with varying luminosity are observed across the horizon of the ASC.

230  
231  
232  
233  
234  
235  
236

The AL index shows that onset of the third substorm occurs at about 22:40 UT. Indeed, at 22:39 UT an auroral arc was observed intensifying from west to east in the very southern horizon of the ASC, indicating the onset was to the west of Scandinavia. Auroral images K and L of Figure 2 show that the radar measured the last ionization enhancement between 22:44 and 22:56 UT when these auroral arcs drift poleward. ASC and narrow FoV keograms indicate that the radar was observing the equatorward edge of an east west aligned auroral arc between 22:53 and 22:56 UT.

237  
238  
239  
240

In addition to ionization by precipitating electrons, sporadic E layers can be seen during two time intervals in the electron density plot. The first sporadic E layer is observed between 20:20 and 20:52 UT in the altitude regions of 109 km, and the second one is between 21:30 and 21:48 UT at about 106 km.

241

#### 4 Electron Energy Spectrum Analysis

242  
243  
244  
245  
246  
247

The analysis method we use to calculate the differential electron energy flux from the EISCAT UHF ISR data consists of two steps. First, plasma parameters are fitted to the incoherent scatter data with high time and range resolutions using the combination of GUIDAP (Lehtinen & Huuskonen, 1996) and BAFIM (Virtanen et al., 2021). Second, the fitted electron density altitude profiles are inverted into differential energy fluxes of precipitating electrons using the ELSPEC software (Virtanen et al., 2018). In

248 this section, we introduce the analysis methods and address the effect of electron heat-  
 249 ing on the raw electron density  $N_r$  for the first substorm discussed in Section 3. We con-  
 250 sider both the bias in raw electron density and its effects on the electron energy spec-  
 251 trum fits.

#### 252 4.1 Fitted and raw electron densities

253 In the traditional 'gated' incoherent scatter plasma parameter fits, one averages  
 254 the incoherent scatter autocorrelation function (ACF) over selected intervals in range  
 255 and time, and fits the plasma parameters to the averaged autocorrelation functions in  
 256 each range-gate and time-step. Each fit is independent of the others and one cannot in-  
 257 clude prior information about shape of the plasma parameter profiles, or about their ex-  
 258 pected temporal variations. Statistical accuracy of the fitted plasma parameters depends  
 259 on the resolutions, since accuracy of the observed ACF is improved with increasing in-  
 260 tegration in time or range. The standard GUISDAP analysis of EISCAT radar data uses  
 261 the gated analysis principle. Accuracy of the GUISDAP fit results depends also on the  
 262 level of ionization in the observed region, which affects the signal-to-noise ratio. Although  
 263 E region electron density is typically high during active aurora, resolutions needed to fol-  
 264 low the associated rapid variations in electron energy spectra are practically out of reach  
 265 of the standard four-parameter fits of  $N_e$ ,  $T_e$ ,  $T_i$ , and  $V_i$  with GUISDAP.

266 Due to the limitations of the four-parameter fits, the high-resolution electron den-  
 267 sity observations are typically based on the raw electron density, which is the backscat-  
 268 tered signal power multiplied with radar system parameters. Assuming that the Debye  
 269 length is much smaller than the radar wavelength, which is a well justified assumption  
 270 in E region observations with the EISCAT UHF radar, the relation between the raw den-  
 271 sity  $N_r$  and the actual density  $N_e$  can be written as (Baron, 1977; Semeter & Kamal-  
 272 abadi, 2005),

$$N_r = \frac{2N_e}{(1 + T_r)}, \quad (1)$$

273 where  $T_r = T_e/T_i$ . Obviously,  $N_e = N_r$  when  $T_r = 1$ , but  $N_e > N_r$  when  $T_r > 1$ . For  
 274 example,  $N_e = 1.5 \cdot N_r$  if  $T_r = 2$ , which is not an unusual temperature ratio in the  
 275 upper E region during electron precipitation. Auroral events with enhanced E region elec-  
 276 tron temperature have been investigated e.g. by Wickwar et al. (1981), who found that  
 277 the electron density altitude profiles calculated with correct temperature ratio have lower  
 278 peak altitudes and greater peak electron densities than those of the raw electron den-  
 279 sity altitude profiles.

280 An alternative to the gated analysis is the full-profile analysis (Holt et al., 1992;  
 281 Lehtinen et al., 1996; Hysell et al., 2008), in which one fits full range-profiles of plasma  
 282 parameters. The full-profile analysis allows one to include prior information about the  
 283 plasma parameter profiles, but it is also computationally heavier than the gated anal-  
 284 ysis. The Bayesian Filtering Module (BAFIM) (Virtanen et al., 2021) is an extension  
 285 module to GUISDAP, which allows one to include prior information about plasma pa-  
 286 rameter gradients in both range and time in the gated GUISDAP analysis. BAFIM thus  
 287 extends the idea of full profile analysis to smoothness in both range and time, but with-  
 288 out increasing the computational burden of the gated analysis. BAFIM introduces cor-  
 289 relations in between adjacent range-gates and time-steps in a way that leads to effectively  
 290 coarser resolutions in range and time than those defined by the range-gates and time-  
 291 steps. Since the correlations are defined for each plasma parameter separately, one can  
 292 use effectively coarser resolutions for  $T_e$ ,  $T_i$ , and  $V_i$ , but fit the electron density  $N_e$  with  
 293 the best possible resolution. The assumption of smoothness in the  $T_e$  and  $T_i$  profiles is  
 294 justified in field-aligned observations, because the high mobility along the magnetic field  
 295 prevents generation of large field-aligned temperature gradients in the upper E and lower  
 296 F regions.

297

## 4.2 High resolution plasma parameter fit with BAFIM

298

299

300

301

302

303

304

305

306

307

308

309

310

311

312

For this study, we ran a BAFIM fit of  $N_e$ ,  $T_e$ ,  $T_i$ , and  $V_i$  on the EISCAT UHF radar data with 1.8 km range steps and 4 s time steps. BAFIM was tuned so that the "effective" time and range resolutions of  $N_e$  are very close to the time and range steps, while resolutions of the other plasma parameters are effectively coarser. Interested readers are referred to Table 1 of Virtanen et al. (2021) for the values of the tuned analysis parameters and their physical meanings. For this particular study, however, we changed the electron density correlation length ( $s^h$ ) and process noise ( $s^t$ ) scaling parameters to 0.1 and  $1.0 \cdot 10^{12} \text{ m}^{-3} \text{ s}^{-1/2}$ , respectively. The 1.8 km resolution was chosen, because it produces better temperature estimates than the 0.9 km resolution, and the change from 0.9 km to 1.8 km resolution did not affect results of the subsequent ELSPEC analysis. The raw electron density is first calculated from the same data with 0.9 km range resolution and 4 s time resolution, and then integrated in range to 1.8 km range resolution to match the corresponding resolution of the BAFIM analysis. The alternating code experiment does not provide true backscattered powers, but the raw density is calculated from a short non-zero lag of the autocorrelation function.

313

314

315

316

317

318

319

320

321

In order to demonstrate the bias in the raw electron density and its subsequent effect on the energy spectra analysis, we choose for the analysis the expansion phase of the first substorm during which pronounced electron heating was observed. The electron density ( $N_e$ ) and temperature ratio ( $T_e/T_i$ ) fit results obtained from the BAFIM analysis are placed in the first and fourth panels of Figure 3, respectively. The raw electron density ( $N_r$ ) is shown in the second panel of the figure. The difference  $N_e - N_r$  is shown in the third panel. As shown in the first and second panels of Figure 3, three intervals of enhanced ionization can be identified from the electron density plots, which are associated to specific auroral features discussed in Section 3.

322

323

324

325

326

327

328

329

330

As shown by the bottom panel of the figure, time intervals with  $T_r > 1$  match with the periods of enhanced ionization. These concurrent enhancements indicate that the energy deposited during the course of precipitation is the cause of the observed electron gas heating. A well established elevation in the electron temperature ( $T_r > 1$ ) can be identified, on average, above about 115 km during all periods of enhanced ionization. In addition,  $T_r$  is shown to increase substantially with altitude to values greater than 1.5 above 130 km during each period of enhanced ionization. Below 103 km we do not fit the temperature ratio, rather we assume  $T_r = 1$ , which is a valid assumption since collision balances the ion and electron temperatures at these altitudes.

331

332

333

334

335

336

337

338

339

The third panel of Figure 3 shows significant differences between the BAFIM electron density and raw electron density estimates during times of electron heating, i.e. when  $T_r > 1$ . Substantial difference (of the order of  $10^{11} \text{ m}^{-3}$ ) can be identified down to 115 km altitude during each period of enhanced ionization. The observed differences increase substantially with altitude and reach about 50% close to 150 km altitude. On the other hand, although the ionization enhancements extend down to 100 km altitude, the difference between BAFIM-fitted and raw electron densities is insignificant below 115 km. This is because frequent collisions balance the electron, ion, and neutral temperatures at these altitudes.

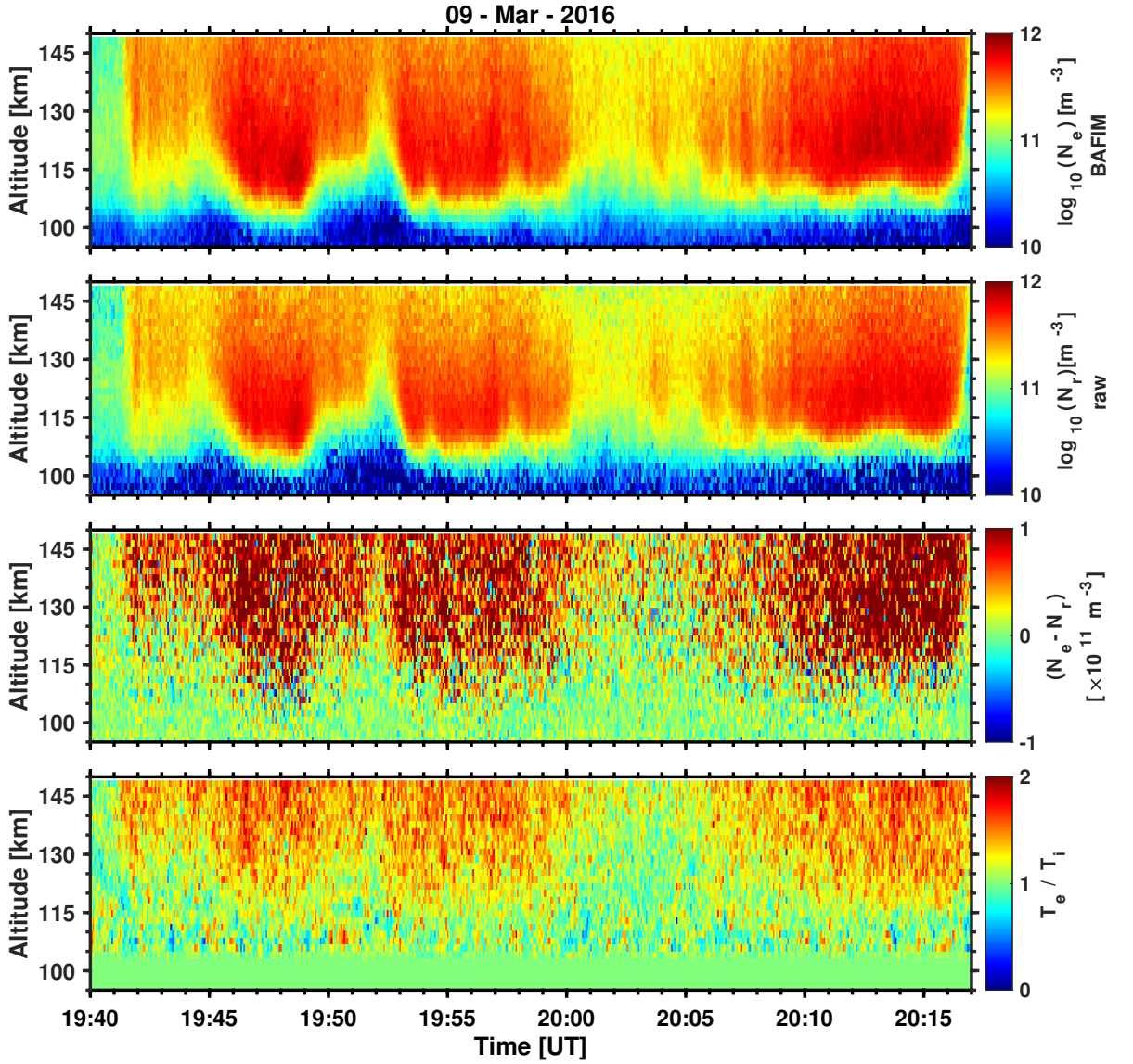


**Figure 3.** Comparison of the raw electron density  $N_r$  and the BAFIM-fitted density  $N_e$ . Panels from top to bottom: BAFIM  $N_e$ , raw density  $N_r$ , Difference  $N_e - N_r$ , and temperature ratio  $T_e/T_i$  from the BAFIM fit.

340

### 4.3 Electron energy spectrum fit with ELSPEC

341

342

343

344

We use the ELSPEC software (Virtanen et al., 2018) to invert the electron density altitude profiles into differential number flux of the precipitating electrons. ELSPEC solves the electron continuity equation that involves the time derivative of the electron density, the ion production ( $Q$ ) and loss ( $L = \alpha N_e^2$ ) rates,

$$\frac{dN_e}{dt} = Q - \alpha N_e^2. \quad (2)$$

345 Ion production by mono-energetic electron beams is calculated using the model of  
 346 Fang et al. (2010), and the ion production by electrons with wide energy spectrum is cal-  
 347 culated as a sum of monoenergetic contributions at selected energy bins. The effective  
 348 recombination coefficient  $\alpha$  as function of ion composition and electron temperature is  
 349 from Sheehan & St.-Maurice (2004), where the ion composition is from the International  
 350 Reference Ionosphere (Bilitza et al., 2017) and the electron temperature is from EISCAT  
 351 ISR measurements. ELSPEC solves the electron density as function of time from the elec-  
 352 tron continuity equation (2), assuming that  $\alpha$  and the electron flux remain constant dur-  
 353 ing a radar integration, and iteratively minimizes the difference between the modeled and  
 354 measured electron density profiles. The fit is performed for a number of different spec-  
 355 trum models in each time step, and the optimal model is selected using the Akaike in-  
 356 formation criterion (Burnham & Anderson, 2002). The technique is targeted for auro-  
 357 ral electrons with energies between 1 and 100 keV, which ionize the atmosphere between  
 358 80 and 150 km altitudes.

359 Originally, ELSPEC used raw electron densities ( $N_r$ ) as input to high resolution  
 360 analysis, because the four-parameter fits were not possible with high resolutions. The  
 361 electron temperature data needed for the recombination speed calculations was taken  
 362 from standard GUIDAP fits with 60 s time and a few km range resolutions, and inter-  
 363 polated to the time and range resolutions of the raw electron density. In this study, we  
 364 use the BAFIM-fitted high-resolution (4 s/1.8 km)  $N_e$  and  $T_e$  as inputs to ELSPEC for  
 365 the first time. In order to study how much the fitted energy spectra change when the  
 366 raw electron density  $N_r$  is replaced with the fitted  $N_e$ , we ran the ELSPEC analysis also  
 367 with the raw density  $N_r$  as input.

#### 368 4.4 Effect of electron heating on energy spectrum fit

369 We applied the ELSPEC analysis on the raw and BAFIM-fitted electron densities  
 370 shown in Figure 3 to demonstrate the effect of electron heating on the electron energy  
 371 spectra fits. This time interval corresponds to the expansion phase of the first substorm  
 372 during which enhanced electron gas heating was observed for several minutes. Figure 4  
 373 shows comparison of the ELSPEC fit results with raw density  $N_r$  and fitted density  $N_e$   
 374 as inputs. From top to bottom, the panels are the BAFIM-fitted electron density ( $N_e$ ),  
 375 the differential energy flux inverted from the BAFIM-fitted electron density ( $I_b$ ), the dif-  
 376 ferential energy flux inverted from the raw electron density ( $I_r$ ), the difference between  
 377  $I_b$  and  $I_r$  ( $I_b - I_r$ ), peak energy ( $E_0$ ), auroral power, and field aligned current (FAC).  
 378 The peak energy is the energy at which the differential energy flux reaches its maximum  
 379 value. The auroral power, which is equal to the total energy flux, is calculated by inte-  
 380 grating the differential energy flux over all energies above 1 keV. The field-aligned cur-  
 381 rent is proportional to the total number flux, which is calculated by integrating the dif-  
 382 ferential number flux. The FAC estimate represents the upward electric current carried  
 383 by the downward precipitating electrons with energies larger than 1 keV. The ELSPEC  
 384 FAC estimates are thus merely lower limits for the total FAC, in which the contribution  
 385 of low-energy electrons could be significant.

386 Comparing the second and third panels of Figure 4, wider energy distribution is  
 387 observed in the energy spectra calculated from BAFIM  $N_e$  than in the one obtained from  
 388 raw density  $N_r$ . Specifically, larger fluxes are observed at lower energies (below about  
 389 5 keV) of  $I_b$  than that of  $I_r$  as shown in the 4<sup>th</sup> panel of the figure. On the other hand,  
 390 the peak energies obtained from raw density  $N_r$  slightly exceed those obtained from BAFIM  
 391  $N_e$  (5<sup>th</sup> panel). This is another indication that the energy distribution obtained from  
 392 BAFIM  $N_e$  tends to have a larger electron flux at its lower energies. The larger flux at  
 393 lower energies of  $I_b$  account for  $N_e > N_r$  above 115 km altitude, as discussed in Sec-  
 394 tion 4.2.

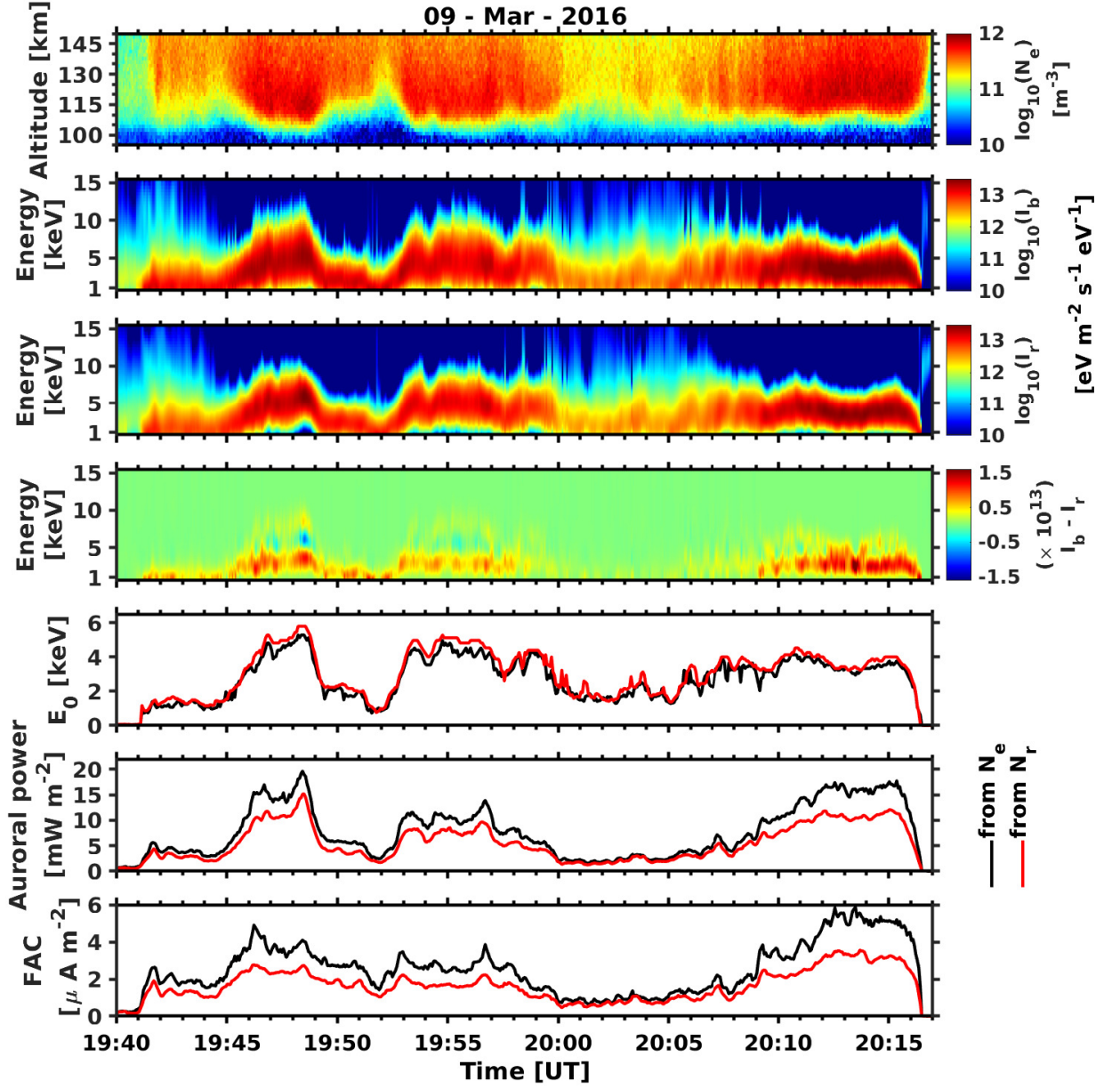


**Figure 4.** Comparison of ELSPEC fit results using raw density  $N_r$  and the BAFIM-fitted density  $N_e$  as inputs. Panels from top to bottom: The BAFIM-fitted  $N_e$ , the differential electron energy fluxes inverted from the BAFIM-fitted  $N_e$  ( $I_b$ ) and raw density ( $I_r$ ), difference between  $I_b$  and  $I_r$  ( $I_b - I_r$ ), peak energies ( $E_0$ ), auroral powers, and field-aligned currents (FAC). In panels 5–7, the black and red curves correspond to the BAFIM-fitted and raw electron density results, respectively.

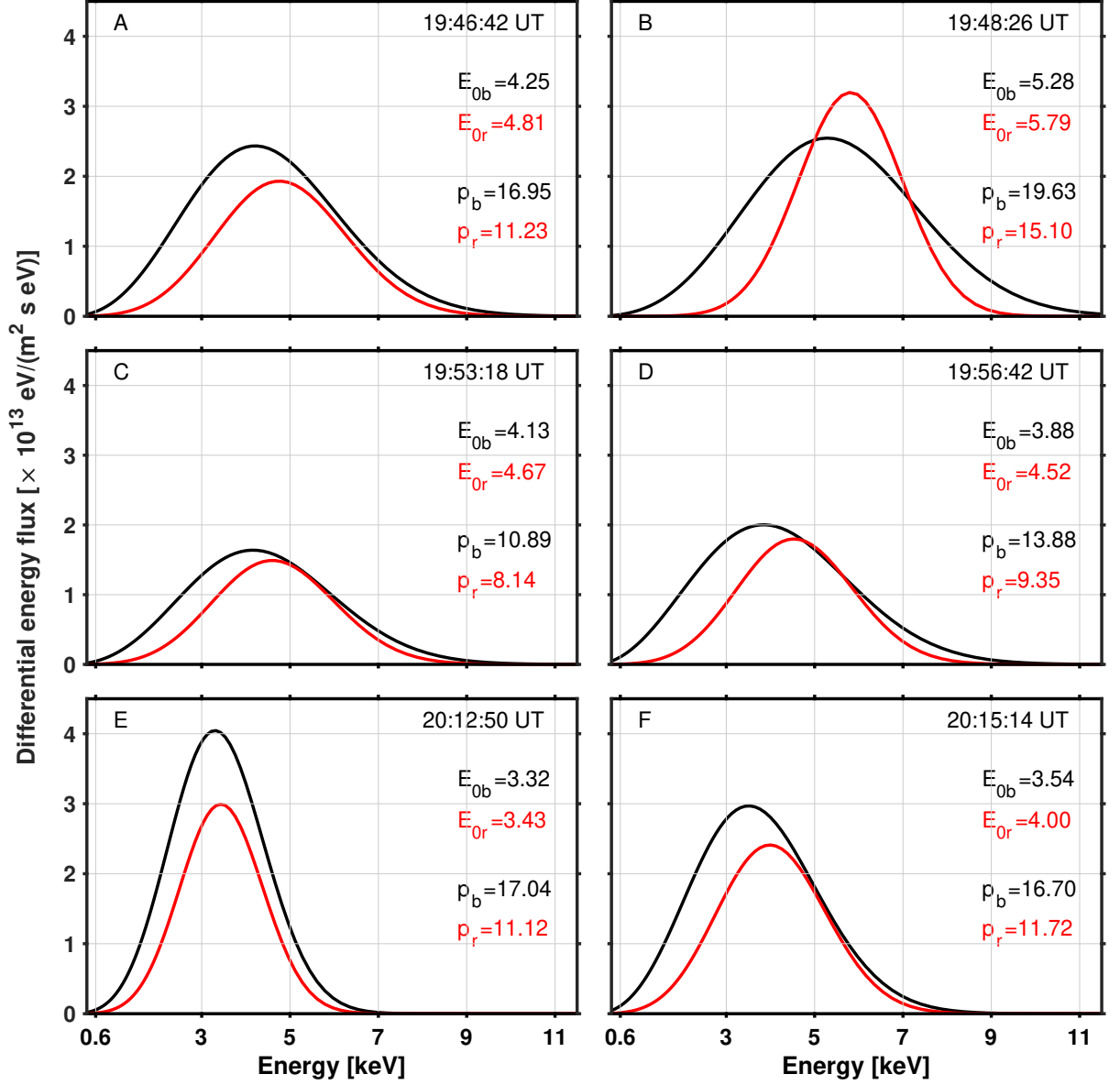


**Figure 5.** Comparison of selected differential energy flux estimates calculated from BAFIM-fitted electron density  $N_e$  (black) and raw electron density  $N_r$  (red).  $E_{ob}$  and  $P_b$  are the peak energies (in keV) and auroral power estimates (in  $\text{mWm}^{-2}$ ) calculated from the BAFIM-fitted  $N_e$ .  $E_{or}$  and  $P_r$  are the corresponding quantities calculated from the raw density  $N_r$ .

395 The 6<sup>th</sup> panel of Figure 4 shows a pronounced difference between the auroral power  
 396 estimates during the first and last periods of enhanced ionization, 19:45–19:48 UT and  
 397 20:09–20:16 UT. During both periods, the auroral power calculated from the BAFIM-  
 398 fitted  $N_e$  exceeds its counterpart calculated from raw density  $N_r$  by about  $5 \text{ mWm}^{-2}$   
 399 (50 %). For the FAC estimates (7<sup>th</sup> panel), the difference is observed for longer time in-  
 400 tervals, 19:45–19:57 UT and 20:09–20:15 UT, during which larger FAC estimate, by about  
 401  $2 \mu\text{Am}^{-2}$  (65%), is derived from the fitted electron density than from the raw electron  
 402 density. In general the total energy flux and number flux estimates obtained from BAFIM  
 403  $N_e$  exceed those obtained from raw density  $N_r$  during each period of enhanced ioniza-  
 404 tion. Detailed distribution of the differences in auroral power and FAC estimates across  
 405 the entire data is discussed in Section 4.5.

406 Figure 5 shows line plots of selected differential energy flux estimates derived from  
 407 the BAFIM-fitted  $N_e$  (black) and raw density  $N_r$  (red). The line plots in panels A–F  
 408 of the figure show energy spectra of the precipitating electrons that produce the corre-  
 409 sponding auroral arcs shown in panels A–F of Figure 2. The peak energies (in keV) and  
 410 auroral power estimates (in  $\text{mWm}^{-2}$ ) at the given time instants are also shown in the  
 411 figure. All the line plots distinctly demonstrate that the differential energy flux calcu-  
 412 lated from the BAFIM-fitted  $N_e$  contains larger energy flux below its peak energy than  
 413 its counterpart calculated from the raw electron density. In addition, the energy spec-  
 414 tra obtained from the raw electron density  $N_r$  shows narrower energy distribution as com-  
 415 pared to its counterpart calculated from the BAFIM-fitted  $N_e$ .

416 BAFIM-ELSPEC analysis results in Figure 5 (black curves) indicate that the bright  
 417 arcs inside the radar beam shown in Figure 2 are produced by precipitating electrons of  
 418 peak energies between 3 and 5 keV. In addition, the total energy flux of the electrons  
 419 that powers the arcs lies in the range between 10 and  $20 \text{ mWm}^{-2}$ . The  $20 \text{ mWm}^{-2}$  au-  
 420 roral power, the largest one here, corresponds to the bright auroral arc observed in the  
 421 early expansion phase of the first substorm, at about 19:48 UT, as shown in Figure 2.

#### 422 4.5 Electron energy spectra from the whole time interval

423 Figure 6 shows different parameters derived from the radar data of the entire event  
 424 that comprises the three substorm activities. In the first and second panels, we have the  
 425 BAFIM-fitted  $N_e$  and the corresponding differential energy flux results, respectively. The  
 426 peak energy, auroral power and FAC estimates are placed in the remaining panels from  
 427 top to bottom. In panels 3–5, the black and red curves represent parameters derived from  
 428 the BAFIM-fitted and raw electron density results, respectively.

429 Several ionization enhancements with different peak altitudes are shown in the elec-  
 430 tron density plot. Ionization enhancements shown before about 21:30 UT have peak alti-  
 431 tudes that lie between 110 and 120 km. Energy distributions of the precipitating elec-  
 432 trons that produce these enhancements were peaking between 3 and 5 keV, as shown in  
 433 the second and third panels. After 21:30 UT, mainly two enhanced ionization periods  
 434 are shown with lowered peak altitudes in the range between 100 and 106 km. The en-  
 435 hancements are produced by hardening of the precipitating electrons whose energies reach  
 436 as large as 21 keV, as shown in the second panel of the figure. The largest peak energy  
 437 and auroral power estimates of the entire event are about 18 keV and  $40 \text{ mWm}^{-2}$ , re-  
 438 spectively, corresponding to the bright and large auroral bulge observed in the post mid-  
 439 night sector during the recovery phase of the second substorm, as illustrated in panel I  
 440 and J of Figure 2. In general, the large ionization enhancements observed before and af-  
 441 ter 21:30 UT are produced by flux of electrons whose peak energy lies in the range 3–  
 442 5 keV, and 5–18 keV, respectively. Moreover, several of the auroral structures observed  
 443 during each substorm event are characterized by inverted-V energy spectra structures.  
 444 The second panel of the figure shows these structures, for example, in the time intervals

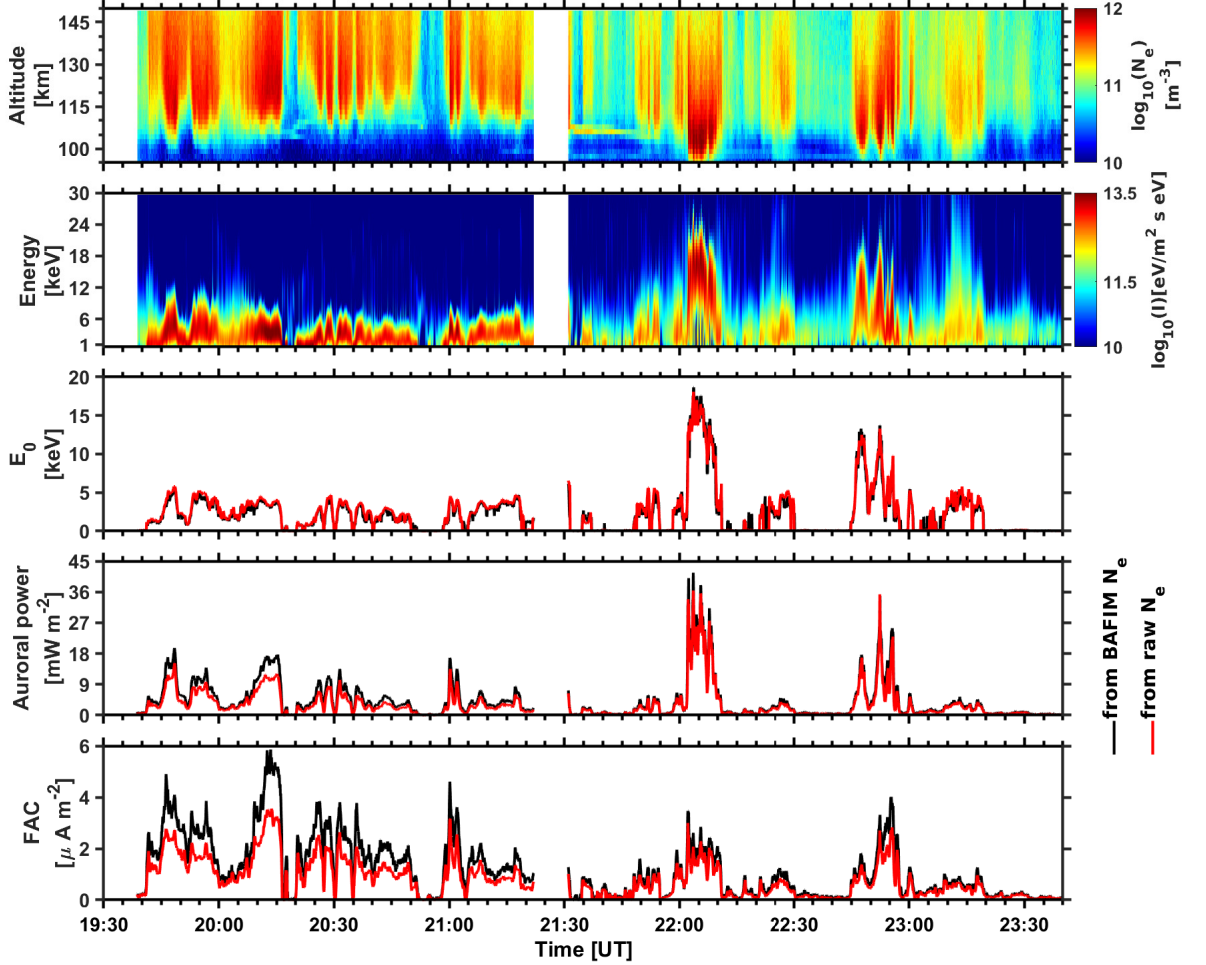


**Figure 6.** ELSPEC fit results during the whole event. Panels from top to bottom: BAFIM-fitted  $N_e$ , differential energy flux, peak energies, auroral powers, and FAC. In panels 3–5, the black and red curves correspond to ELSPEC analysis results using the BAFIM-fitted  $N_e$  and raw density  $N_r$ , respectively

445 19:45–19:50 UT, 22:01–22:10 UT and 22:45–23:00 UT, owing to rapid motion of auro-  
 446 ral arcs across the radar beam as detailed in Section 3.

447 The inference from the bottom two panels of Figure 6 is that the auroral power and  
 448 FAC estimates obtained from the BAFIM-fitted  $N_e$  significantly exceed their counter-  
 449 parts obtained from the raw density  $N_r$ , during the first substorm before 21:30 UT. How-  
 450 ever, during the last two substorm periods after 21:30, the differences become smaller.  
 451 This is because, before 21:30 UT large flux of lower energy electrons deposit their en-  
 452 ergy at higher altitudes and heat the electron gas above the ion temperature. Whereas  
 453 for those periods after 21:30 UT, the electrons become sufficiently energetic and cause  
 454 enhanced ionization below 115 km altitude, where collisions balance the ion and elec-  
 455 tron temperatures. Electron temperature was sometimes higher than ion temperature  
 456 at high altitudes ( $> 120$  km) after 21:30 UT, but this has a relatively small effect on  
 457 the derivation of auroral power and FAC because peaks of the electron density altitude  
 458 profiles were at lower altitudes.

459 Figure 7 presents distribution of the actual and percentage difference between the  
 460 auroral powers (left panel) and FAC (right panel) calculated from  $N_e$  and  $N_r$  data of the  
 461 whole time interval (4 hours). The differences are calculated only for time instances at  
 462 which the auroral power calculated from  $N_r$  is greater than  $3 \text{ mWm}^{-2}$ . The histograms  
 463 show that the differences between the auroral power estimates peak in the range  $0.5\text{--}$   
 464  $2.5 \text{ mWm}^{-2}$  (30–45 %). For the FAC estimates, the peak difference is in the range  $0.25\text{--}$   
 465  $0.5 \mu\text{Am}^{-2}$  (45–55 %). The largest differences between the auroral power estimates is  
 466 about 75 %. In general, the histograms show that the auroral power and FAC estimates  
 467 calculated from  $N_e$  typically exceed those from  $N_r$ , but most of the times the difference  
 468 is smaller than those extreme cases discussed in Section 4.4.

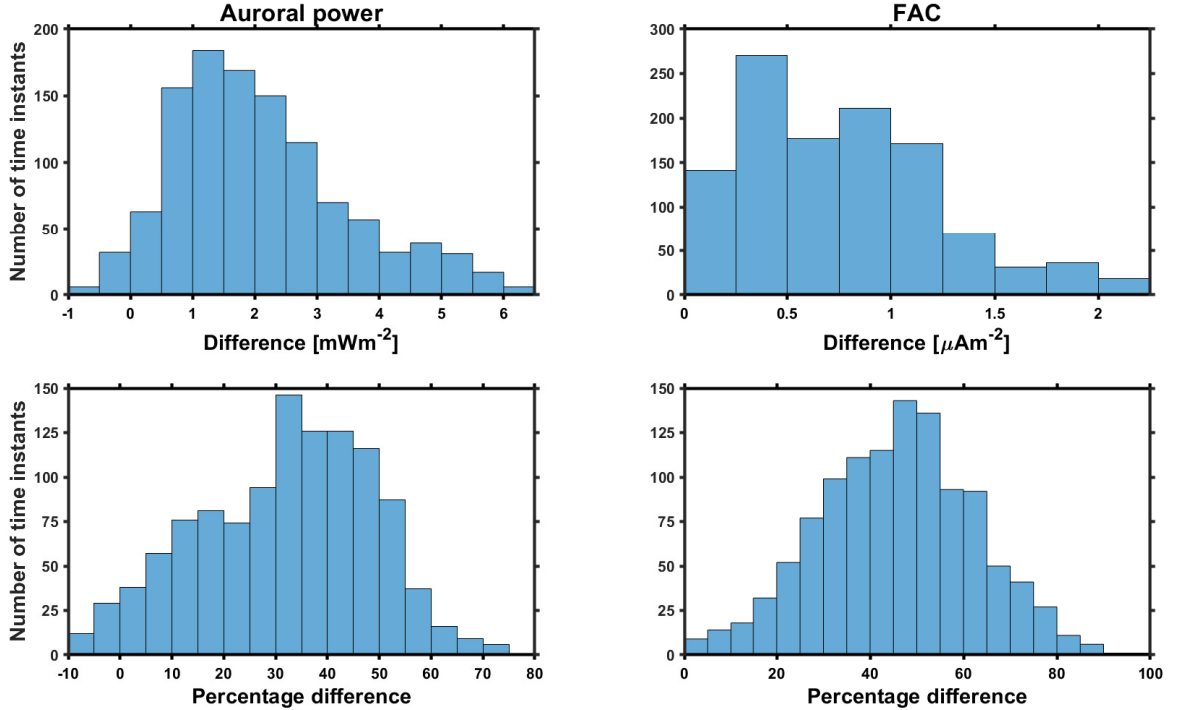


**Figure 7.** Distribution of the absolute and percentage differences in the auroral power (left panels) and FAC (right panels) estimates.

## 469 5 Comparison to optical observations

### 470 5.1 Auroral power from radar and blue molecular band emission intensity

472 We validate our radar analysis results by means of comparing radar observations  
 473 of auroral power with simultaneous, co-located observation of the blue 427.8 nm emis-  
 474 sion intensity, utilizing their proportionality relationship. The emission intensity data  
 475 used in this study is in arbitrary pixel count units without being corrected for dark cur-  
 476 rent leakage in the detectors (Nel, 2019), possible contributions from night time air-glow  
 477 emission, and atmospheric scattering of light from nearby sources. We subtract the back-  
 478 ground and scale the emission intensities to the same units with the radar data by means  
 479 of a linear least-square fit between the auroral power and the blue line emission inten-  
 480 sity. The emission intensity used in the linear fit is the median intensity of five pixels

481 found inside the radar beam. Equation 3 and Figure 8 show results of the linear fit be-  
 482 tween the blue line emission data and auroral power estimates calculated from BAFIM-  
 483 fitted  $N_e$ .

$$P = 0.0042I_{4278} - 3.8333, \quad (3)$$

484 where  $P$  is in  $\text{mWm}^{-2}$  and the constant term is attributed to the background data sources  
 485 in the optical data. Figure 8 demonstrates a very good linear relationship between the  
 486 427.8 nm emission intensity and the total energy flux of the precipitating electrons. For  
 487 this particular event, we calculated a cross-correlation coefficient value of 0.96 between  
 488 the auroral power and the 427.8 nm emission intensity.

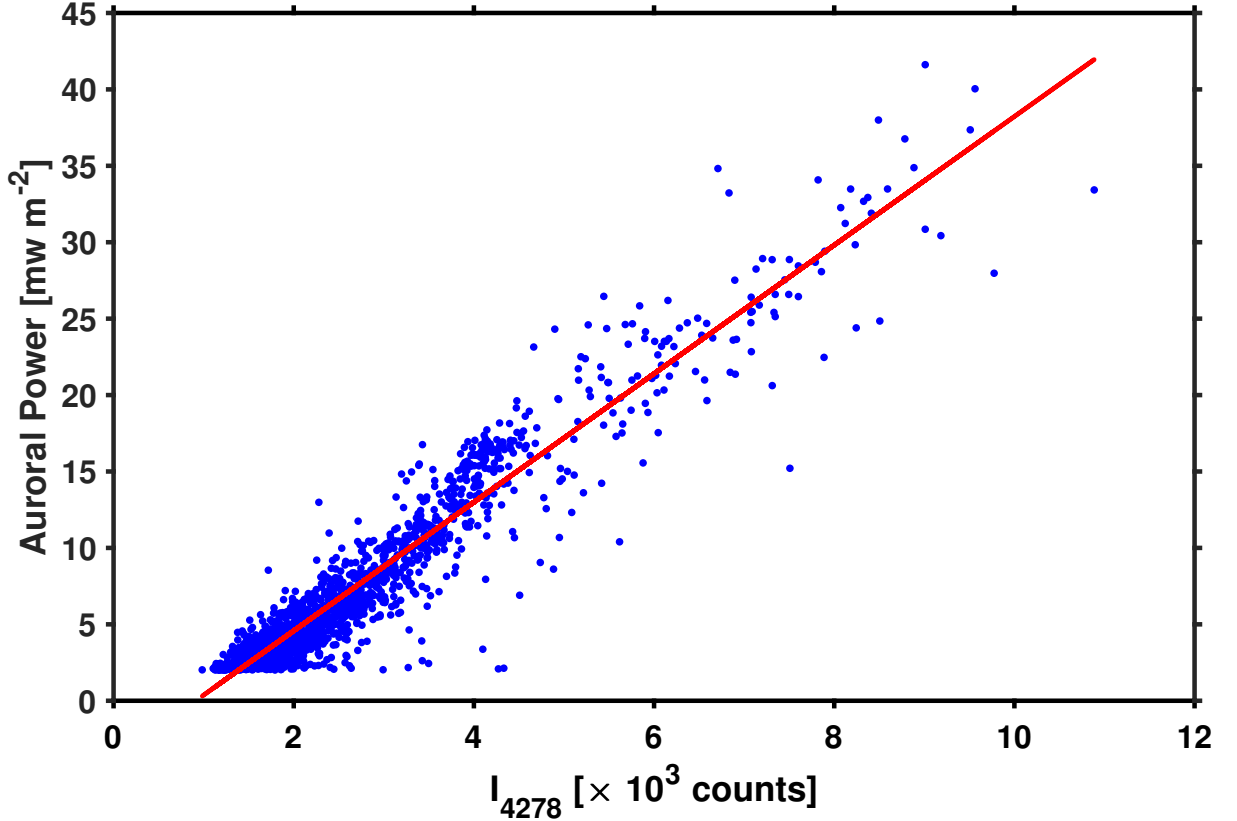


**Figure 8.** Fitting the blue line emission data to the auroral power calculated by ELSPEC using the BAFIM fitted electron density.

489 Comparison between the temporal variations of the scaled 427.8 nm emission in-  
 490 tensity and the auroral power is shown in the top panel of Figure 9. As shown in the fig-  
 491 ure, both large scale and small scale variations of the 427.8 nm emission intensity match  
 492 very well with variations in auroral power calculated from radar data. Furthermore, sharp  
 493 temporal gradients in the emission intensity are captured by the auroral power calcu-  
 494 lated from the radar data using the BAFIM-fitted electron density. By "sharp gradients"  
 495 we refer to variations in time-scales of the radar integration (4 s) in this context. Effects  
 496 of precipitation flux variations during a radar integration are discussed in Section 5.2.  
 497

498 There are some instances when the scaled emission intensity is smaller than the au-  
 499 roral power calculated from the radar data. This happens, for example, between 20:11

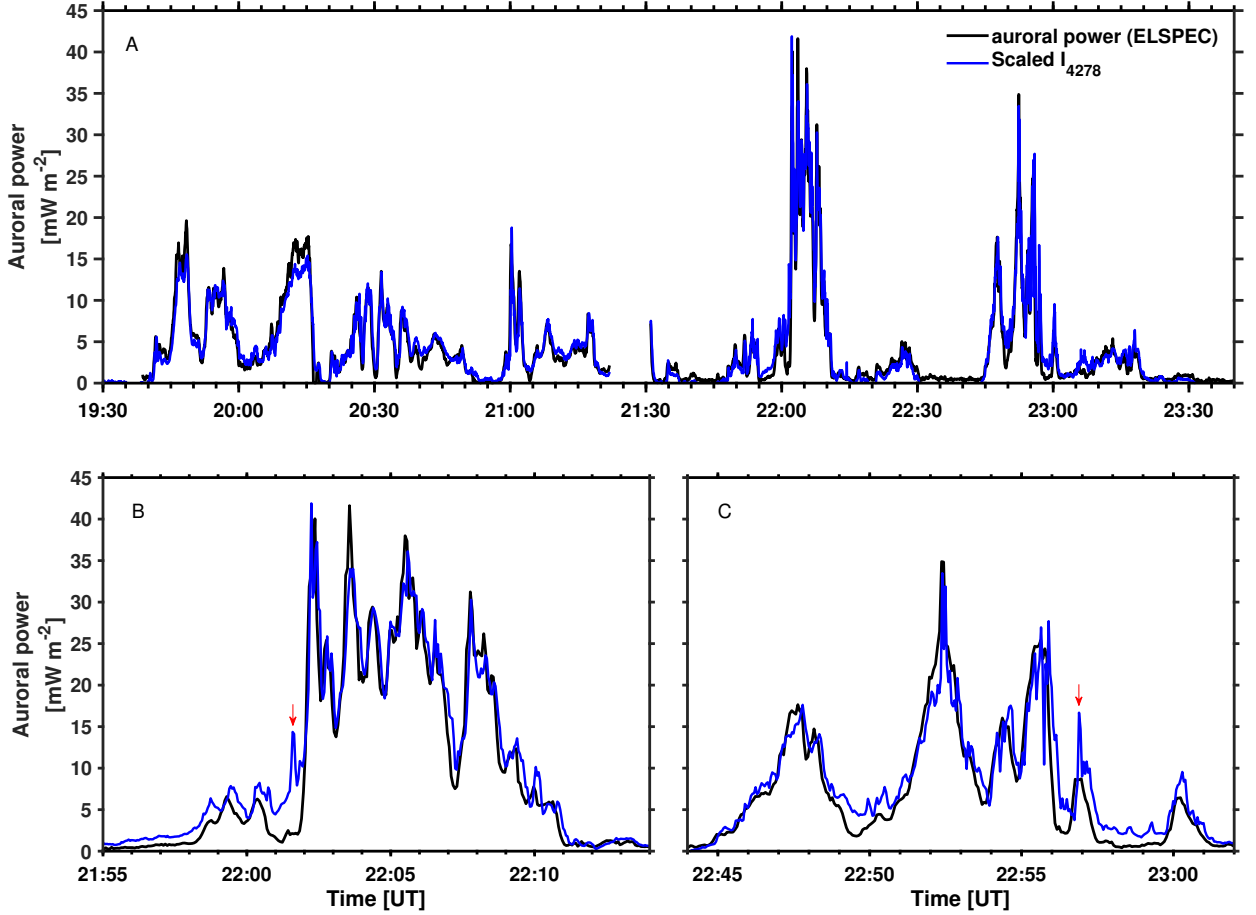


**Figure 9.** Panel A: Comparing the temporal variations of the auroral power (black) and the scaled emission intensity (blue). Panels B and C: selected periods from panel A.

500 and 20:15 UT when the flux of about 1 keV electrons was large. Previous studies have  
 501 shown that the prompt emission rate of blue photons per unit deposited energy decreases  
 502 with altitude and characteristic energy of the depositing electrons (Rees & Luckey, 1974;  
 503 Partamies et al., 2004). As a result, our scaled 427.8 nm emission intensities might be  
 504 underestimates of the auroral power during these time intervals. Another potential cause  
 505 of the discrepancy is overestimation of the auroral power by ELSPEC due to ion com-  
 506 position variations. The effect of ion composition variations was studied by Virtanen et  
 507 al. (2018), who found that the Sodankylä Ion and Neutral Chemistry (SIC) model (Tu-  
 508 runen et al., 2016) predicts enhanced and rapidly varying  $O_2^+$  to  $NO^+$  ion ratios dur-  
 509 ing electron precipitation, and ELSPEC analysis with  $O_2^+$  to  $NO^+$  ion ratio taken from  
 510 the International Reference Ionosphere (Bilitza et al., 2017) produced up to 20% larger  
 511 auroral powers than the corresponding analysis using SIC ion compositions in an event  
 512 study.

## 513 5.2 Effect of narrow auroral structures on ELSPEC analysis

514 Figure 9 also shows a few instances when the scaled emission intensity is clearly  
 515 larger than the auroral power calculated from radar data. For better visualization, se-  
 516 lected parts of the comparison graph which contain these time instants are shown sep-

517 arately in panels B and C of the Figure. Centered at each time instant, narrow FoV au-  
 518 roral images from three subsequent 3 s exposure times are shown in Figure 10. The first  
 519 one occurs between 22:01:35 UT and 22:01:41 UT (indicated by a red arrow in panel B  
 520 of Figure 9) when a thin auroral structure with rapidly varying intensity is within the  
 521 radar beam, as shown in the top panels of Figure 10. The images indicate that the radar  
 522 beam is not filled uniformly by the arc before and after 22:01:38 UT. In addition, a satel-  
 523 lite crossed the radar beam at 22:01:41, and light reflected from the satellite contributes  
 524 to the observed emission intensity. The satellite is marked with blue arrows in the Fig-  
 525 ure. Panel C of Figure 9 shows the next significant discrepancy at around 22:56:53 UT  
 526 (indicated by a red arrow), when the equatorward edge of an east west elongated arc en-  
 527 ters the radar beam and returns back within a time scale shorter than the radar inte-  
 528 gration time, as shown in the bottom panels of Figure 10.

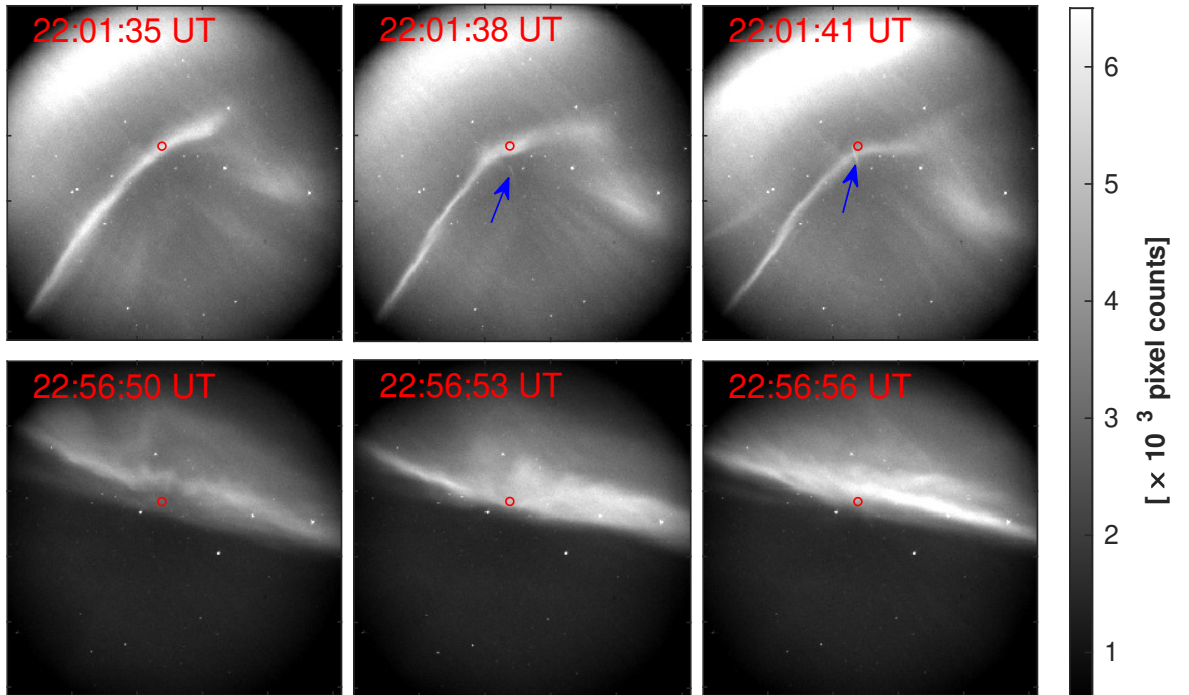


**Figure 10.** Narrow FoV auroral images at the given instants of time. The red circle represent the radar beam and the arrows indicate to a passing satellite.

529 The small scale structures and rapid variations are a probable reason for the dif-  
 530 ferences in these cases. The comparison between radar and optical data breaks down when  
 531 the fields of view are not uniformly filled (Lanchester et al., 1997) or when the aurora  
 532 are more dynamic than the available time resolution. In the radar analysis, violating the  
 533 implicit assumption of uniform energy flux within the radar beam and during the radar  
 534 integration time readily leads to underestimation of the total flux. The same effect has  
 535 been demonstrated by Tuttle et al. (2014) and was discussed also by Dahlgren et al. (2011).

## 536 6 Discussion and Summary

537 This study demonstrates for the first time the applicability of a novel combination  
 538 of two analysis methods (BAFIM and ELSPEC) for estimation of precipitating electron

energy spectra, auroral power, and upward FAC from incoherent scatter radar measurements. The unique advantages of this combined analysis is utilization of the fitted electron density, instead of the raw electron density, with high time and range resolutions as input for the ELSPEC analysis. This removes a bias caused by electron heating that may have existed in previous high time resolution ISR observations which have relied on the raw electron density. Accurate electron energy spectra estimates are crucial for studies of small-scale, rapidly varying auroras, and incoherent scatter radars are currently the best available instruments for such observations.

The BAFIM-ELSPEC analysis method is applied to an auroral event containing three small substorms that occur in the pre-midnight and post-midnight sectors on 9 March 2016. The four-parameter fits of  $N_e$ ,  $T_e$ ,  $T_i$ , and  $V_i$  to the E region EISCAT UHF ISR data were performed with 4 s / 1.8 km resolutions by using the Bayesian Filtering Module (BAFIM) (Virtanen et al., 2021). We find that  $N_r$  is systematically smaller than  $N_e$  in the E region when electron precipitation heats the electron gas above the ion temperature. The effect is largest at the top of the E region, where  $N_e$  is up to 50 % larger than  $N_r$  above 130 km altitude, but significant differences are also observed down to 115 km.

When the fitted  $N_e$  is used in electron energy spectrum fits with ELSPEC (Virtanen et al., 2018), wider energy spectra and larger total fluxes are produced than in the corresponding analysis with  $N_r$  as input. Larger number fluxes are produced at the low energy end of the spectra in particular. Auroral power (total energy flux) integrated from the fitted energy spectra is up to 75 % larger than the estimates calculated with  $N_r$  as input. However, the distribution of the difference peaks at lower values between 30–45 %. Similarly, the upward FAC estimate is typically 45–55 % higher when the fitted  $N_e$  is used instead of the raw electron density. These results indicate that previous studies that have relied on the raw electron density may have significantly underestimated the auroral power and upward field-aligned current carried by the precipitating electrons.

Significant differences between the auroral power estimates are observed during the expansion phase of the first substorm which occurred in the pre-midnight sector in connection to flux of precipitating electrons with peak energies between 3 and 5 keV. The differences become insignificant when the precipitating electrons are sufficiently energetic to produce ionization at lower altitudes, in this study below 115 km. This happens, in this study, corresponding to the post-midnight auroral activities during the second and third substorm periods. The auroral power estimates corresponding to observed ionization enhancements during the night of 9 March 2016 were in the range of 3–40  $\text{mWm}^{-2}$ . These values are in accordance with several other previous studies (Stenbaek-Nielsen et al., 1998; Dahlgren et al., 2011; Kaeppler et al., 2015). The largest auroral power of the night, 40  $\text{mWm}^{-2}$ , was associated with a bright auroral bulge observed in the post-midnight sector as a result of precipitating electrons with peak energies as large as 18 keV.

The auroral powers calculated using the BAFIM-ELSPEC analysis combination were compared to column intensities of the optical 427.8 nm emission to validate the estimates. A linear correlation between the two were found, and the temporal evolution showed an excellent match. A few significant discrepancies during short time periods were found, but those were shown to correspond to situations when auroral structures narrower than the radar beam move across the beam, or when the electron energy spectrum changes considerably during a radar integration. In these cases, the observed discrepancies indicate that structures narrower than the radar beam and variations in time-scales shorter than the radar integration lead to underestimation of the total electron flux in ELSPEC.

Only electrons with energies larger than 1 keV are included in the estimates of auroral power and FAC in this study. ELSPEC cannot reliably estimate electron fluxes at lower energies, because the low-energy electrons produce ionization above 150 km altitude, where plasma convection and concentration of the long-lived  $O^+$  ions may be sig-

591 nificant. Ionization by the low-energy electrons can be seen in F region ISR measure-  
 592 ments, but it cannot be reliably used for the energy spectra inversion. As a consequence,  
 593 the FAC estimates of ELSPEC are merely lower limits, because contribution of low-energy  
 594 electrons to the total FAC could be significant. The auroral power estimates are expected  
 595 to be less affected, since the energy flux is typically dominated by auroral electrons with  
 596 energy greater than 1 keV.

597 Strong electric fields are sometimes known to exist adjacent to auroral arcs in the  
 598 ionosphere and they typically point toward the arc center (Lanchester et al., 1996; Aikio  
 599 et al., 2002). In the F region, the corresponding ion drifts take place along the auroral  
 600 arc, but with decreasing altitude the ion velocity turns more and more in the direction  
 601 of electric field due to Pedersen mobility in the E region, which means that the plasma  
 602 in the low density region outside of the arc may intrude to the more dense plasma in-  
 603 side the arc. This kind of behavior has been observed as an electron density depletion  
 604 around 125 km altitude by (Dahlgren et al., 2011) at the trailing edge of an arc. Such  
 605 density depletion would be incorrectly interpreted as very fast recombination by ELSPEC.  
 606 However, in the future, we will be able to measure the 2D horizontal plasma drift pat-  
 607 tern in the E and F regions by the EISCAT\_3D radar (McCrea et al., 2015) and take into  
 608 account the advection term in the continuity equation.

609 The present work uses 4 s time resolution due to limitations of the BAFIM-GUISDAP  
 610 software combination. Without this limitation we should be able to match the time res-  
 611 olution with duration of the alternating code cycle, which is 0.44 s in case of the arc1  
 612 experiment. It is also technically possible to run ELSPEC with sub-second resolution  
 613 data. As a matter of fact, the 0.44 s resolution energy spectra published by (Dahlgren  
 614 et al., 2011) were calculated by a software that was used as a starting point for ELSPEC  
 615 development.

## 616 Acknowledgments

617 We acknowledge the EISCAT Association for the incoherent scatter radar data used in  
 618 this study. EISCAT is an international association supported by research organisations  
 619 in China (CRIRP), Finland (SA), Japan (NIPR and ISEE), Norway (NFR), Sweden (VR),  
 620 and the United Kingdom (UKRI). EISCAT data are available for download from [https://  
 621 portal.eiscat.se/schedule/](https://portal.eiscat.se/schedule/). The auroral blue line emission intensity data used in  
 622 this study is available at <https://figshare.com/s/bf5482eb4a1f6bd0fc0a>, and quick-  
 623 look images for the Watec monochromatic imager (WMI) can be accessed from [http://  
 624 pc115.seg20.nipr.ac.jp/www/AQVN/index.html](http://pc115.seg20.nipr.ac.jp/www/AQVN/index.html). We thank T. Raita, Sodankylä Geo-  
 625 physical Observatory, Finland, for the Kilpisjärvi Pulsation magnetometer data. We thank  
 626 the institutes who maintain the IMAGE Magnetometer Array: Tromsø Geophysical Ob-  
 627 servatory of UiT the Arctic University of Norway (Norway), Finnish Meteorological In-  
 628 stitute (Finland), Institute of Geophysics Polish Academy of Sciences (Poland), GFZ Ger-  
 629 man Research Centre for Geosciences (Germany), Geological Survey of Sweden (Swe-  
 630 den), Swedish Institute of Space Physics (Sweden), Sodankylä Geophysical Observatory  
 631 of the University of Oulu (Finland), and Polar Geophysical Institute (Russia). The im-  
 632 age magnetometer network data is available at [https://space.fmi.fi/image/www/index  
 633 .php?page=user\\_defined](https://space.fmi.fi/image/www/index.php?page=user_defined). The authors would like to thank the World Data Center for  
 634 Geomagnetism (Kyoto) for the AL index data at [http://wdc.kugi.kyoto-u.ac.jp/  
 635 aeasy/index.html](http://wdc.kugi.kyoto-u.ac.jp/aeasy/index.html). This work is supported by the Academy of Finland (301542) and  
 636 the Kvantum institute of the University of Oulu.

## 637 References

638 Aikio, A. T., Lakkala, T., Kozlovsky, A., & Williams, P. J. S. (2002). Electric fields  
 639 and currents of stable drifting auroral arcs in the evening sector. *Journal of Geo-  
 640 physical Research: Space Physics*, 107(A12), SIA 3-1-SIA 3-14. doi: <https://doi>

- 641 .org/10.1029/2001JA009172
- 642 Baron, M. J. (1977). The chatanika radar system. In A. Brekke (Ed.), *Radar probing*  
643 *of the auroral plasma* (p. 103-141). Tromsø, Norway: Universitetsforlaget.
- 644 Bilitza, D., Altadill, D., Truhlik, V., Shubin, V., Galkin, I., Reinisch, B., & Huang,  
645 X. (2017). International Reference Ionosphere 2016: From ionospheric cli-  
646 mate to real-time weather predictions. *Space Weather*, *15*(2), 418-429. doi:  
647 10.1002/2016SW001593
- 648 Brekke, A., Hall, C., & Hansen, T. L. (1989, June). Auroral ionospheric conduc-  
649 tances during disturbed conditions. *Annales Geophysicae*, *7*, 269-280.
- 650 Burnham, K. P., & Anderson, D. R. (2002). *Model Selection and Multimodel Infer-*  
651 *ence* (2nd ed.). Springer.
- 652 Burns, C., Howarth, W., & Hargreaves, J. (1990). High-resolution incoherent  
653 scatter radar measurements during electron precipitation events. *Journal of At-*  
654 *mospheric and Terrestrial Physics*, *52*(3), 205 - 218. doi: [https://doi.org/10.1016/](https://doi.org/10.1016/0021-9169(90)90124-6)  
655 [0021-9169\(90\)90124-6](https://doi.org/10.1016/0021-9169(90)90124-6)
- 656 Carlson, C. W., Pfaff, R. F., & Watzin, J. G. (1998). The Fast auroral snapshot  
657 (FAST) mission. *Geophysical Research Letters*, *25*(12), 2013-2016. doi: [https://doi](https://doi.org/10.1029/98GL01592)  
658 [.org/10.1029/98GL01592](https://doi.org/10.1029/98GL01592)
- 659 Dahlgren, H., Gustavsson, B., Lanchester, B. S., Ivchenko, N., Brändström,  
660 U., Whiter, D. K., ... Marklund, G. (2011). Energy and flux variations  
661 across thin auroral arcs. *Annales Geophysicae*, *29*(10), 1699-1712. doi:  
662 <https://doi.org/10.5194/angeo-29-1699-2011>
- 663 Dombeck, J., Cattell, C., Prasad, N., Meeker, E., Hanson, E., & McFadden, J.  
664 (2018). Identification of auroral electron precipitation mechanism combina-  
665 tions and their relationships to net downgoing energy and number flux. *Jour-*  
666 *nal of Geophysical Research: Space Physics*, *123*(12), 10,064-10,089. doi:  
667 <https://doi.org/10.1029/2018JA025749>
- 668 Fang, X., Randall, C. E., Lummerzheim, D., Wang, W., Lu, G., Solomon, S. C., &  
669 Frahm, R. A. (2010). Parameterization of monoenergetic electron impact ion-  
670 ization. *Geophysical Research Letters*, *37*(22). doi: [https://doi.org/10.1029/](https://doi.org/10.1029/2010GL045406)  
671 [2010GL045406](https://doi.org/10.1029/2010GL045406)
- 672 Fujii, R., Nozawa, S., Sato, M., Matuura, N., Ono, T., Brekke, A., ... Hansen,  
673 T. L. (1995). Comparison between electron spectra calculated from EISCAT  
674 electron density profiles and those observed by the DMSF satellites. *Journal of*  
675 *geomagnetism and geoelectricity*, *47*(8), 771-782. doi: [https://doi.org/10.5636/](https://doi.org/10.5636/jgg.47.771)  
676 [jgg.47.771](https://doi.org/10.5636/jgg.47.771)
- 677 Hargreaves, J., & Devlin, T. (1990). Morning sector electron precipitation events  
678 observed by incoherent scatter radar. *Journal of Atmospheric and Terrestrial*  
679 *Physics*, *52*(3), 193 - 203. doi: [https://doi.org/10.1016/0021-9169\(90\)90123-5](https://doi.org/10.1016/0021-9169(90)90123-5)
- 680 Holt, J. M., Rhoda, D. A., Tetenbaum, D., & van Eyken, A. P. (1992, May-June).  
681 Optimal analysis of incoherent scatter radar data. *Radio Sci.*, *27*(3), 435-447. doi:  
682 <https://doi.org/10.1029/91RS02922>
- 683 Hsu, T.-S., & McPherron, R. L. (2012). A statistical analysis of substorm associated  
684 tail activity. *Advances in Space Research*, *50*(10), 1317-1343. doi: [https://doi.org/](https://doi.org/10.1016/j.asr.2012.06.034)  
685 [10.1016/j.asr.2012.06.034](https://doi.org/10.1016/j.asr.2012.06.034)
- 686 Hysell, D. L., Rodrigues, F. S., Chau, J. L., & Huba, J. D. (2008). Full profile in-  
687 coherent scatter analysis at Jicamarca. *Ann. Geophys.*, *26*, 59-75. doi: [10.5194/](https://doi.org/10.5194/angeo-26-59-2008)  
688 [angeo-26-59-2008](https://doi.org/10.5194/angeo-26-59-2008)
- 689 Kaeppler, S. R., Hampton, D. L., Nicolls, M. J., Strømme, A., Solomon, S. C.,  
690 Hecht, J. H., & Conde, M. G. (2015). An investigation comparing ground-based  
691 techniques that quantify auroral electron flux and conductance. *Journal of Geo-*  
692 *physical Research: Space Physics*, *120*(10), 9038-9056. doi: [https://doi.org/](https://doi.org/10.1002/2015JA021396)  
693 [10.1002/2015JA021396](https://doi.org/10.1002/2015JA021396)
- 694 Kallio, E. I., Pulkkinen, T. I., Koskinen, H. E. J., Viljanen, A., Slavin, J. A., &

- 695 Ogilvie, K. (2000). Loading-unloading processes in the nightside ionosphere.  
 696 *Geophysical Research Letters*, *27*(11), 1627-1630. doi: [https://doi.org/10.1029/](https://doi.org/10.1029/1999GL003694)  
 697 [1999GL003694](https://doi.org/10.1029/1999GL003694)
- 698 Kirkwood, S. (1988). *SPECTRUM: A computer algorithm to derive the flux-energy*  
 699 *spectrum of precipitating particles from EISCAT electron density profiles.*
- 700 Kirkwood, S., & Eliasson, L. (1990). Energetic particle precipitation in the sub-  
 701 storm growth phase measured by EISCAT and Viking. *Journal of Geophysi-*  
 702 *cal Research: Space Physics*, *95*(A5), 6025-6037. doi: [https://doi.org/10.1029/](https://doi.org/10.1029/JA095iA05p06025)  
 703 [JA095iA05p06025](https://doi.org/10.1029/JA095iA05p06025)
- 704 Kosch, M. J., Honary, F., del Pozo, C. F., Marple, S. R., & Hagfors, T. (2001).  
 705 High-resolution maps of the characteristic energy of precipitating auroral particles.  
 706 *Journal of Geophysical Research: Space Physics*, *106*(A12), 28925-28937. doi:  
 707 <https://doi.org/10.1029/2001JA900107>
- 708 Lanchester, B. S., Kaila, K., & McCrea, I. W. (1996). Relationship between  
 709 large horizontal electric fields and auroral arc elements. *Journal of Geophysi-*  
 710 *cal Research: Space Physics*, *101*(A3), 5075-5084. doi: [https://doi.org/10.1029/](https://doi.org/10.1029/95JA02055)  
 711 [95JA02055](https://doi.org/10.1029/95JA02055)
- 712 Lanchester, B. S., Palmer, J. R., Rees, M. H., Lummerzheim, D., Kaila, K., &  
 713 Turunen, T. (1994). Energy flux and characteristic energy of an elemen-  
 714 tal auroral structure. *Geophysical Research Letters*, *21*(25), 2789-2792. doi:  
 715 <https://doi.org/10.1029/94GL01764>
- 716 Lanchester, B. S., Rees, M. H., Lummerzheim, D., Otto, A., Frey, H. U., & Kaila,  
 717 K. U. (1997). Large fluxes of auroral electrons in filaments of 100 m width.  
 718 *Journal of Geophysical Research: Space Physics*, *102*(A5), 9741-9748. doi:  
 719 <https://doi.org/10.1029/97JA00231>
- 720 Lehtinen, M. S., & Häggström, I. (1987). A new modulation principle for incoher-  
 721 ent scatter measurements. *Radio Sci.*, *22*, 625-634. doi: [https://doi.org/10.1029/](https://doi.org/10.1029/RS022i004p00625)  
 722 [RS022i004p00625](https://doi.org/10.1029/RS022i004p00625)
- 723 Lehtinen, M. S., & Huuskonen, A. (1996). General incoherent scatter analysis and  
 724 GUIDAP. *Journal of Atmospheric and Terrestrial Physics*, *58*(1), 435 - 452. doi:  
 725 [https://doi.org/10.1016/0021-9169\(95\)00047-X](https://doi.org/10.1016/0021-9169(95)00047-X)
- 726 Lehtinen, M. S., Huuskonen, A., & Pirttilä, J. (1996, December). First experi-  
 727 ences of full-profile analysis with GUIDAP. *Ann. Geophys.*, *14*, 1487-1495. doi:  
 728 <https://doi.org/10.1007/s00585-996-1487-3>
- 729 McCrea, I., Aikio, A., Alfonsi, L., Belova, E., Buchert, S., Clilverd, M., ... Vierinen,  
 730 J. (2015). The science case for the EISCAT 3D radar. *Prog. Earth Planet. Sc.*,  
 731 *2*(1). doi: [10.1186/s40645-015-0051-8](https://doi.org/10.1186/s40645-015-0051-8)
- 732 McPherron, R. L. (2005, Sep 01). Magnetic pulsations: Their sources and relation to  
 733 solar wind and geomagnetic activity. *Surveys in Geophysics*, *26*(5), 545-592. doi:  
 734 [10.1007/s10712-005-1758-7](https://doi.org/10.1007/s10712-005-1758-7)
- 735 Mishin, V. V., Tsegmed, B., Klivanova, Y. Y., & Kurikalova, M. A. (2020). Burst  
 736 geomagnetic pulsations as indicators of substorm expansion onsets during storms.  
 737 *Journal of Geophysical Research: Space Physics*, *125*(10), e2020JA028521. doi:  
 738 <https://doi.org/10.1029/2020JA028521>
- 739 Nel, A. E. (2019). *Novel radar and optical observations of black auroras in the upper*  
 740 *atmosphere* (Doctoral dissertation, North-West University). [https://repository](https://repository.nwu.ac.za/handle/10394/35266)  
 741 [.nwu.ac.za/handle/10394/35266](https://repository.nwu.ac.za/handle/10394/35266).
- 742 Nel, A. E., Kosch, M. J., Whiter, D., Gustavsson, B., & Aslaksen, T. (2021, Jan 19).  
 743 A new auroral phenomenon, the anti-black aurora. *Scientific Reports*, *11*(1), 1829.  
 744 doi: <https://doi.org/10.1038/s41598-021-81363-9>
- 745 Newell, T., Sotirelis, T., & Wing, S. (2009). Diffuse, monoenergetic, and broadband  
 746 aurora: The global precipitation budget. *Journal of Geophysical Research: Space*  
 747 *Physics*, *114*(A9). doi: <https://doi.org/10.1029/2009JA014326>
- 748 Nose, M., Iyemori, T., Sugiura, M., & Kamei, T. (2015). *AE Index*. WDC for Geo-

- 749 magnetism, Kyoto. doi: 10.17593/15031-54800
- 750 Ogawa, Y., Tanaka, Y., Kadokura, A., Hosokawa, K., Ebihara, Y., Motoba, T.,  
751 ... Fujii, R. (2020). Development of low-cost multi-wavelength imager  
752 system for studies of aurora and airglow. *Polar Science*, *23*, 100501. doi:  
753 <https://doi.org/10.1016/j.polar.2019.100501>
- 754 Olson, J. V. (1999). Pi2 pulsations and substorm onsets: A review. *Journal of Geo-*  
755 *physical Research: Space Physics*, *104*(A8), 17499-17520. doi: <https://doi.org/10.1029/1999JA900086>
- 756
- 757 Omholt, A. (1971). The electron aurora: Main characteristics and luminosity. In  
758 *Physics and chemistry in space* (p. 24–46). Springer Berlin Heidelberg. doi: 10  
759 .1007/978-3-642-46269-6.2
- 760 Osepian, A., & Kirkwood, S. (1996). High-energy electron fluxes derived from EIS-  
761 CAT electron density profiles. *Journal of Atmospheric and Terrestrial Physics*,  
762 *58*(1), 479 - 487. doi: [https://doi.org/10.1016/0021-9169\(95\)00050-X](https://doi.org/10.1016/0021-9169(95)00050-X)
- 763 Partamies, N., Janhunen, P., Kauristie, K., Mäkinen, S., & Sergienko, T. (2004).  
764 Testing an inversion method for estimating electron energy fluxes from all-sky  
765 camera images. *Annales Geophysicae*, *22*(6), 1961–1971. doi: <https://doi.org/10.5194/angeo-22-1961-2004>
- 766
- 767 Raita, T., & University of Oulu. (2022). *Horizontal power spectrum of the finnish*  
768 *pulsation magnetometer data from kilpisjärvi on 9.3.2016*. University of Oulu, So-  
769 dankylä Geophysical Observatory.
- 770 Rees, M. H. (1963). Auroral ionization and excitation by incident energetic elec-  
771 trons. *Planetary and Space Science*, *11*(10), 1209 - 1218. doi: [https://doi.org/10.1016/0032-0633\(63\)90252-6](https://doi.org/10.1016/0032-0633(63)90252-6)
- 772
- 773 Rees, M. H., & Luckey, D. (1974). Auroral electron energy derived from ratio of  
774 spectroscopic emissions 1. Model computations. *Journal of Geophysical Research*  
775 *(1896-1977)*, *79*(34), 5181-5186. doi: <https://doi.org/10.1029/JA079i034p05181>
- 776 Saito, T. (1969, December). Geomagnetic Pulsations. *Space Science Review*, *10*(3),  
777 319–412. doi: <https://doi.org/10.1007/BF00203620>
- 778 Sakurai, T., & Saito, T. (1976). Magnetic pulsation pi2 and substorm onset.  
779 *Planetary and Space Science*, *24*(6), 573 - 575. doi: [https://doi.org/10.1016/0032-0633\(76\)90135-5](https://doi.org/10.1016/0032-0633(76)90135-5)
- 780
- 781 Semeter, J., & Kamalabadi, F. (2005). Determination of primary electron spectra  
782 from incoherent scatter radar measurements of the auroral E region. *Radio Sci-*  
783 *ence*, *40*(2). doi: <https://doi.org/10.1029/2004RS003042>
- 784 Sheehan, C. H., & St.-Maurice, J.-P. (2004). Dissociative recombination of  
785  $N_2^+$ ,  $O_2^+$ , and  $NO^+$ : Rate coefficients for ground state and vibrationally ex-  
786 cited ions. *Journal of Geophysical Research: Space Physics*, *109*(A3). doi:  
787 <https://doi.org/10.1029/2003JA010132>
- 788 Simon Wedlund, C., Lamy, H., Gustavsson, B., Sergienko, T., & Brändström, U.  
789 (2013). Estimating energy spectra of electron precipitation above auroral arcs  
790 from ground-based observations with radar and optics. *Journal of Geophysi-*  
791 *cal Research: Space Physics*, *118*(6), 3672-3691. doi: [https://doi.org/10.1002/](https://doi.org/10.1002/jgra.50347)  
792 [jgra.50347](https://doi.org/10.1002/jgra.50347)
- 793 Stenbaek-Nielsen, H. C., Hallinan, T. J., Osborne, D. L., Kimball, J., Chaston, C.,  
794 McFadden, J., ... Carlson, C. W. (1998). Aircraft observations conjugate to  
795 FAST: Auroral arc thicknesses. *Geophysical Research Letters*, *25*(12), 2073-2076.  
796 doi: <https://doi.org/10.1029/98GL01058>
- 797 Strickland, D. J., Hecht, J. H., Christensen, A. B., & Kelly, J. (1994). Relationship  
798 between energy flux Q and mean energy E of auroral electron spectra based on  
799 radar data from the 1987 CEDAR campaign at Sondre Stromfjord, Greenland.  
800 *Journal of Geophysical Research: Space Physics*, *99*(A10), 19467-19473. doi:  
801 <https://doi.org/10.1029/94JA01901>
- 802 Strickland, D. J., Meier, R. R., Hecht, J. H., & Christensen, A. B. (1989). Deducing

- 803 composition and incident electron spectra from ground-based auroral optical mea-  
804 surements: Theory and model results. *Journal of Geophysical Research*, 94(A10),  
805 13527. doi: <https://doi.org/10.1029/ja094ia10p13527>
- 806 Tanskanen, E. I. (2009). A comprehensive high-throughput analysis of substorms  
807 observed by IMAGE magnetometer network: Years 1993–2003 examined. *Journal*  
808 *of Geophysical Research: Space Physics*, 114(A5). doi: [https://doi.org/10.1029/](https://doi.org/10.1029/2008JA013682)  
809 2008JA013682
- 810 Turunen, E., Kero, A., Verronen, P. T., Miyoshi, Y., Oyama, S.-I., & Saito, S.  
811 (2016). Mesospheric ozone destruction by high-energy electron precipitation  
812 associated with pulsating aurora. *J. Geophys. Res. Atmos.*, 121, 11852-11861. doi:  
813 10.1002/2016JD025015
- 814 Tuttle, S., Gustavsson, B., & Lanchester, B. (2014). Temporal and spatial evo-  
815 lution of auroral electron energy spectra in a region surrounding the magnetic  
816 zenith. *Journal of Geophysical Research: Space Physics*, 119(3), 2318-2327. doi:  
817 <https://doi.org/10.1002/2013JA019627>
- 818 Virtanen, I. I., Gustavsson, B., Aikio, A., Kero, A., Asamura, K., & Ogawa, Y.  
819 (2018). Electron energy spectrum and auroral power estimation from incoherent  
820 scatter radar measurements. *Journal of Geophysical Research: Space Physics*,  
821 123(8), 6865-6887. doi: 10.1029/2018JA025636
- 822 Virtanen, I. I., Tesfaw, H. W., Roininen, L., Lasanen, S., & Aikio, A. (2021).  
823 Bayesian filtering in incoherent scatter plasma parameter fits. *Journal of Geo-*  
824 *physical Research: Space Physics*, 126(3), e2020JA028700. doi: [https://doi.org/](https://doi.org/10.1029/2020JA028700)  
825 10.1029/2020JA028700
- 826 Vondrak, R. R., & Baron, M. J. (1977). A method of obtaining the energy dis-  
827 tribution of auroral electrons from incoherent scatter radar measurements. In  
828 A. Brekke (Ed.), *Radar probing of the auroral plasma* (p. 315-330). Tromsø,  
829 Norway: Universitetsforlaget.
- 830 Wickwar, V. B., Lathuillere, C., Kofman, W., & Lejeune, G. (1981). Elevated elec-  
831 tron temperatures in the auroral E layer measured with the chatanika radar. *Jour-*  
832 *nal of Geophysical Research: Space Physics*, 86(A6), 4721-4730. doi: [https://doi](https://doi.org/10.1029/JA086iA06p04721)  
833 [.org/10.1029/JA086iA06p04721](https://doi.org/10.1029/JA086iA06p04721)